Check for updates

Paleoceanography and Paleoclimatology

RESEARCH ARTICLE
10.1029/2020PA003993

Key Points:

- The onset of Asian dust is identified at 40 Ma within a longer continuous record
- Shifts in the dust, cyclostratigraphy and pollen suggest the Siberian High at 40 Ma
- The coeval proto-Paratethys Sea retreat triggered the onset of the Siberian High

Supporting Information:

- Supporting Information S1
- Data Set S1
- Data Set S2
- Data Set S3
- Data Set S4

Correspondence to:
N. Meijer,
niels.meijer@senckenberg.de

Citation:
Meijer, N., Dupont-Nivet, G., Barbolini, N., Woutersen, A., Rohrmann, A., Zhang, Y., et al. (2021). Loess-like dust appearance at 40 Ma in central China. *Paleoceanography and Paleoclimatology*, *36*, e2020PA003993. https://doi.org/10.1029/2020PA003993

Received 2 JUN 2020
Accepted 29 JAN 2021

© 2021. The Authors.
This is an open access article under the terms of the Creative Commons Attribution License, which permits use, distribution and reproduction in any medium, provided the original work is properly cited.

Loess-Like Dust Appearance at 40 Ma in Central China

Niels Meijer[1], Guillaume Dupont-Nivet[1,2,3], Natasha Barbolini[4,5], Amber Woutersen[5], Alexander Rohrmann[6], Yang Zhang[3], Xiang-Jun Liu[7], Alexis Licht[8], Hemmo A. Abels[9], Carina Hoorn[5], Rik Tjallingii[10], Christoff Andermann[10], Michael Dietze[10], and Norbert Nowaczyk[10]

[1]Institute for Geosciences, Universität Potsdam, Potsdam, Germany, [2]Univ Rennes, CNRS, Géosciences Rennes - UMR CNRS 6118, Rennes, France, [3]Key Laboratory of Orogenic Belts and Crustal Evolution, Ministry of Education, School of Earth and Space Sciences, Peking University, Beijing, China, [4]Department of Ecology, Environment and Plant Sciences and Bolin Centre for Climate Research, Stockholm University, Stockholm, Sweden, [5]Department of Ecosystem and Landscape Dynamics (ELD), Institute for Biodiversity and Ecosystem Dynamics (IBED), University of Amsterdam, Amsterdam, The Netherlands, [6]Institute of Geological Sciences, Freie Universität Berlin, Berlin, Germany, [7]College of Geography and Environmental Science, Northwest Normal University, Lanzhou, China, [8]Department of Earth and Space Sciences, University of Washington, Seattle, WA, USA, [9]Department of Geosciences and Engineering, Delft University of Technology, Delft, The Netherlands, [10]GFZ German Research Centre for Geosciences, Potsdam, Germany

Abstract Asian mineral dust has been studied extensively for its role in affecting regional-to global-scale climate and for its deposits, which enable reconstructing Asian atmospheric circulation in the past. However, the timing and origin of the dust deposits remain debated. Numerous loess records have been reported across the Asian continent with ages varying from the Miocene to the Eocene and linked to various mechanisms including global cooling, Tibetan Plateau uplift and retreat of the inland proto-Paratethys Sea. Here, we study the Eocene terrestrial mudrocks of the Xining Basin in central China and use nonparametric end-member analysis of grain-size distributions to identify a loess-like dust component appearing in the record at 40 Ma. This is coeval with the onset of high-latitude orbital cycles and a shift to predominant steppe-desert vegetation as recognized by previous studies in the same record. Furthermore, we derive wind directions from eolian dune deposits which suggest northwesterly winds, similar to the modern-day winter monsoon which is driven by a high pressure system developing over Siberia. We propose that the observed shifts at 40 Ma reflect the onset of the Siberian High interacting with westerly derived moisture at obliquity timescales and promoting dust storms and aridification in central China. The timing suggests that the onset may have been triggered by increased continentality due to the retreating proto-Paratethys Sea.

1. Introduction

During wintertime, the Asian continent is characterized by a high atmospheric pressure system developing over southern Siberia and Mongolia. This semi-permanent high-pressure system known as the Siberian High drives strong northwesterly winds of the modern-day East Asian winter monsoon bringing cold and dry air from the Asian interior (Chang et al., 2006). During springtime, the Siberian High creates a strong meridional temperature contrast between cold air in the north and warmer air in the lower mid-latitudes that can result in frequent dust storms (Roe, 2009). These storms transport silt-sized material (with median grain-sizes of 20–60 μm) from the arid upwind areas to the Chinese Loess Plateau located downwind (J. Sun, 2002). This Plateau provides a unique record for studying the history of Asian aridification and atmospheric circulation (Maher, 2016). Furthermore, the transported mineral dust plays an important role in cooling the atmosphere by scattering solar radiation, promoting cloud formation and providing nutrients to the Pacific Ocean (Jickells et al., 2005; Martin, 1990; Shaffer & Lambert, 2018).

Identifying the onset of the Chinese dust deposits is key to better understand the origin of the East Asian atmospheric circulation and the role of mineral dust in the evolution of regional-to global-scale climate. However, various ages for the onset of dust deposition (Figure 1a) have been reported so far spanning from Pliocene to Eocene epochs (Ao et al., 2016; Z. L. Ding et al., 1998; 2001; Garzione et al., 2005; Guo et al., 2002; Jiang & Ding, 2010; Li et al, 2018; Licht et al., 2014; X. Qiang et al., 2011; Y. Song et al., 2001; D. Sun et al., 1997; D. Sun, Shaw, et al., 1998; D. Sun, An, et al., 1998; Xu et al., 2009; Y. Zhang et al., 2014;

Zheng et al., 1992; Y. Zhu et al., 2008). The classic sequence of Quaternary loess initiated at ~2.6 Ma and is linked to the coeval glaciation of the Northern Hemisphere (Z. Ding et al., 1997; Lu et al., 2010). These loess deposits are interbedded with finer-grained reddish paleosols (median grain-sizes of 10–30 μm) formed during interglacials, which are interpreted to have formed under a wetter East Asian summer monsoon (Maher, 2016). Conformably underlying the Quaternary loess is the Red Clay, which, despite the name, consists mostly of silt-sized material similar to the paleosols in the Quaternary loess. These are interpreted to reflect the atmospheric circulation during the warmer and wetter Miocene-Pliocene epochs (Maher, 2016). In the central Chinese Loess Plateau, east of the Liupan Shan, ages of the Red Clay range between 7 and 11 Ma (Ao et al., 2016; Z. L. Ding et al., 1998; 2001; B. Wang, Zheng, et al., 2014; Y. Song et al., 2001; D. Sun et al., 1997; D. Sun, Shaw, et al., 1998; D. Sun, An, et al., 1998; Xu et al., 2009; Zheng et al., 1992; Y. Zhu et al., 2008). The onset of these dust deposits is interpreted as the set-up of winter monsoonal circulation and inland aridification both linked to the uplift of the Tibetan Plateau (An et al., 2001). However, older loess-like deposits extending up to ~20–29 Ma were identified west of the Liupan Shan (Garzione et al., 2005; Guo et al., 2002; X. Qiang et al., 2011; Y. Zhang et al., 2014) and to the north of the Loess Plateau (Jiang & Ding, 2010). These records suggest that the monsoonal circulation is much older and proposed to be driven by the combined effect of an earlier phase of Tibetan Plateau uplift and the retreat of the inland Paratethys Sea that covered the Eurasian continent during the Paleogene (Guo et al., 2002). In recent years, even older dust deposits have been identified in Eocene strata (Li et al., 2018; Licht et al., 2014), suggesting that Asian atmospheric circulation may have been driven by the India-Asia collision, greenhouse to icehouse cooling or proto-Paratethys Sea incursions, all occurring during the Eocene.

Some of the oldest loess-like deposits in central China have been identified in the Eocene mudrocks of the Xining Basin (Figure 1) and are shown to extend from 34 Ma to at least 40 Ma (Licht et al., 2014). These deposits have been used as an indicator for aridity and winter monsoonal circulation (Licht et al., 2014). However, it remains unclear when dust deposition started in the basin which has important implications for the origin of Asian dust and associated atmospheric circulation. Moreover, recent sedimentological and provenance studies show that the pre-Quaternary dust records in central China contain significant contributions from local fluvial sources which obscures the dust signal (Alonso-Zarza et al., 2009; Liu et al., 2019; Nie et al., 2014; Y. Zhang et al., 2014; H. Zhang et al., 2018).

Here, we reassess and extend the sedimentary record of Licht et al. (2014) to ~50.5 Ma using multiple previously dated sections in the Xining Basin as well as a new sedimentary section (Baimasi) containing widespread eolian sedimentary structures of deflated gypsum grains to derive paleo-wind directions (Figure 1b). Using these sections, we construct a composite record of grain-size distributions (GSDs) to identify windblown dust in the mudrocks. The measured GSDs of these mudrocks represent a mix of the different fluvial and eolian components operating in the basin. These are subsequently unmixed using a nonparametric end-member analysis to quantify the relative contributions of eolian dust (Paterson & Heslop, 2015; van Hateren et al., 2018; Varga, Újvári, & Kovács, 2019). End-member modeling of GSDs has been successfully applied to distinguish eolian and fluvial contributions in marine cores (e.g., Weltje and Prins, 2003) as well as lacustrine records (e.g., Dietze et al., 2014) and in various other sedimentary environments (e.g., see appendix I in van Hateren et al., 2018). In addition, the end-member models have been extensively tested and shown to perform well using both artificial and natural data sets (Dietze & Dietze, 2019; Paterson & Heslop, 2015; van Hateren et al., 2018; Varga, Gresina, et al., 2019). Using this approach, we identify a loess-like dust component appearing in the record at ~40 Ma, coeval with the onset of obliquity-forced atmospheric moisture cycles and an increase in steppe-desert vegetation previously recognized in the Xining Basin by Bosboom et al. (2014). We subsequently extend both the cyclostratigraphic and palynological records to the early Eocene with additional samples which corroborate the previous findings of Bosboom et al. (2014), but propose an alternative interpretation involving the onset of the Siberian High at 40 Ma.

2. Geologic Setting and Previous Work

The modern-day Xining Basin is bounded by the eastern Qilian Shan in the north, the Laji Shan in the south and the Riyue Shan in the west. The basin constitutes the westernmost part of the Cenozoic Longzhong Basin, which stretches toward the Liupan Shan in the east (Horton et al., 2004). Various tectonic settings have

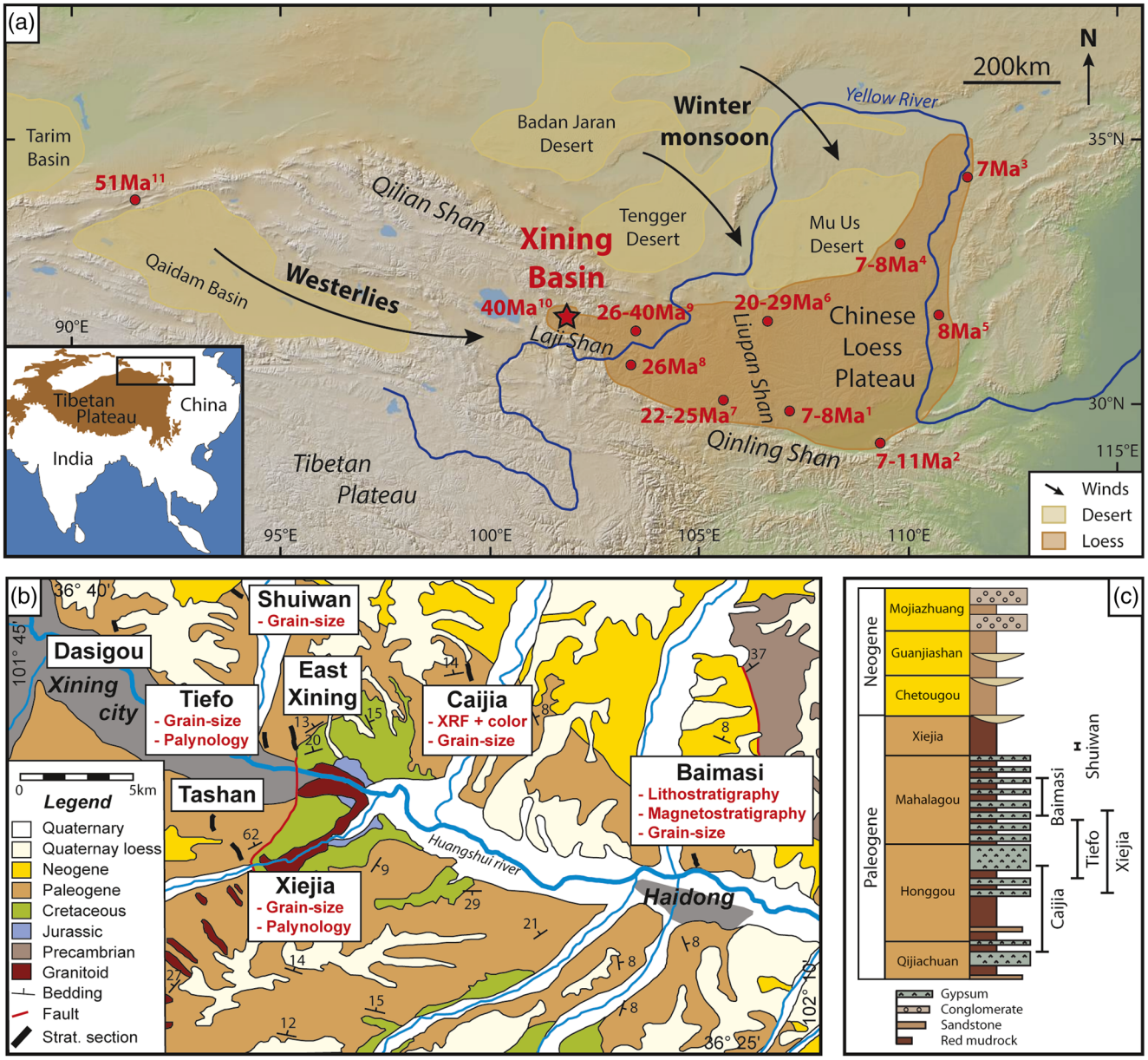

Figure 1. Modern-day topographic map (http://www.geomapapp.org) of the northeastern Tibetan Plateau showing various reported ages for the onset of loess-like deposits (modified from Meijer et al., 2020): (1) central Loess Plateau: Z. L. Ding et al. (2001); Y. Song et al. (2001); D. Sun et al. (1997); D. Sun, Shaw, et al. (1998); D. Sun, An, et al. (1998); (2) southern Loess Plateau: Zheng et al. (1992); D. Sun et al. (1997); Wang et al. (2014); (3) Baode: Y. Zhu et al. (2008); (4) Jiaxian: Ding et al. (1998); Qiang et al. (2001); (5) Shilou: Xu et al. (2009); age reinterpreted by Ao et al. (2016); (6) Sikouzi: Jiang et al. (2010); age reinterpreted by W. T. Wang et al. (2011); (7) Tianshui Basin: Guo et al. (2002); record extended by X. Qiang et al. (2011); (8) Linxia Basin: Garzione et al. (2005); (9) Lanzhou Basin: Y. Zhang et al. (2014); age reinterpreted by W. Wang et al. (2016); (10) Xining Basin: Licht et al. (2014); (11) Xorkol Basin (Li et al., 2018). The Xining Basin is indicated with a star. (b) Geological map of the Xining Basin based on BGMRQP (1965), QBGMR (1985), and Dai et al. (2006) showing the locations of the sections in the Xining Basin. Datasets generated in this study are indicated in red. (c) Lithostratigraphy listing the formations of the Xining Basin adapted from Horton et al. (2004) and updated following Fang et al. (2019). Stratigraphic intervals covered by the datasets of this study are indicated on the right.

been proposed for the Paleogene Xining Basin, including a foreland basin of the western Qinling Shan (Liu et al., 2013), a strike-slip basin due to differential rotation of crustal blocks (J. Zhang, Wang, et al., 2016) or an extensional basin due to the far-field effect of the subducting Pacific plate (L. G. Fan et al., 2019). During the Neogene, the Longzhong Basin was segmented into smaller subbasins due to deformation of the northeastern Tibetan Plateau (Horton et al., 2004).

2.1. Lithostratigraphy

Cenozoic deposition commenced during the early Eocene and unconformably overlies Cretaceous strata or older basement rocks (L. G. Fan et al., 2019; Fang et al., 2019). Paleogene deposits include the Qijiachuan, Honggou, Mahalagou and Xiejia Formations (BGMRQP, 1965; Dai et al., 2006; Horton et al., 2004; QBGMR, 1985 and Figure 1c). The Qijiachuan Formation consists of organic-rich evaporites and fluvio-lacustrine mudrocks (Fang et al., 2019; Meijer et al., 2019). These are followed by brick-red, massive mudrocks of the Honggou Formation alternated with lacustrine mudrocks containing carbonate beds and evaporites (Meijer et al., 2019). Fluvial sandstones are found locally in the lower part, but decrease upwards (Meijer et al., 2019). The Honggou Formation successions are interpreted mainly as a dry mudflat in a distal alluvial environment based on the occurrence of evaporites and the massive structure of the mudrocks resulting from subaerial reworking such as bioturbation and pedogenesis (Meijer et al., 2019). The overlying Mahalagou Formation is characterized by orbitally forced alternations between massive red mudrocks and gypsum beds (Abels et al., 2011; Dupont-Nivet et al., 2007; G. Q. Xiao et al., 2010 and Figure 2a). The gypsum beds in the Xining Basin disappear after the Eocene-Oligocene Transition (EOT) due to regional aridification (Dupont-Nivet et al., 2007). The uppermost gypsum bed at the EOT is used as a stratigraphic marker for the boundary to the Oligocene Xiejia Formation composed predominantly of brownish-red mudrocks (Fang et al., 2019).

Neogene formations include the brownish-yellow alluvial mudrocks and fluvial sandstones of the Chetougou and Guanjiashan Formations and the conglomerates of the Mojiazhuang Formation (Fang et al., 2019; R. Yang et al., 2017; W. Zhang et al., 2017). The Neogene deposits are upwardly coarsening due to increased uplift of the eastern Qilian Shan, located north of the Xining Basin (Fang et al., 2019; R. Yang et al., 2017), and of the Laji Shan located to the south (G. Xiao et al., 2012). Subsequent incision of the Huangshui River resulted in fluvial terraces which are capped by up to 200 m of Pliocene Red Clay and Quaternary loess (Fang et al., 2019; W. Zhang et al., 2017).

2.2. Previous Work

Previous studies in the Xining Basin have interpreted the massive mudrocks of the Eocene Mahalagou Formation as loess-like dust (Licht et al., 2014). This interpretation is based on the surface textures of the silt-sized quartz grains indicating eolian transport, the GSDs of the mudrocks being similar to Quaternary loess and the lack of sedimentary structures indicative of fluvial deposition (Licht et al., 2014). In addition, the U-Pb age spectra of detrital zircons indicate a provenance similar to the Quaternary Chinese loess (Licht et al., 2016). It has also been noted that the meter-scale cycles in the Mahalagou Formation between gypsum beds and mudrocks may be the Eocene equivalent of the orbitally driven loess-paleosol alternations observed in the Quaternary records of the Chinese Loess Plateau (Licht et al., 2014).

These Eocene cycles are observed in the center of the Xining Basin (at the Dasigou, Shuiwan, Tiefo, East Xining, Tashan and Xiejia sections; Figure 1b) and are identified as predominantly driven by the 41-kyr obliquity cycle and to a minor extent by the 100-kyr eccentricity cycle (Abels et al., 2011; Dupont-Nivet et al., 2007; Huang & Hinnov, 2019; G. Q. Xiao et al., 2010). The gypsum beds are interpreted as wet periods with an elevated groundwater level, whereas the red mudrocks reflect a dry mudflat (Abels et al., 2011; Dupont-Nivet et al., 2007). Bosboom et al. (2014) identified the onset of these cycles at 40 Ma after a brief transitional phase between ~40.5 and 40 Ma which is characterized by laterally discontinuous gypsum beds, which become continuous afterward. In addition, Bosboom et al. (2014) proposed that the onset of these cycles correlates with an increased prevalence of steppe-desert vegetation observed via the pollen record, but this was poorly constrained between 40.7 and 39.5 Ma due to a lack of productive palynological samples in this interval.

Both the onset of obliquity cycles and the increased dominance of steppe-desert vegetation have been linked to aridification due to global cooling shortly after the Middle Eocene Climatic Optimum (MECO; Bosboom et al., 2014). However, a recent study using clumped isotopes identified no atmospheric cooling in the Xining Basin at 40 Ma (Page et al., 2019) thereby challenging this interpretation. The stratigraphic record in the Xining Basin has subsequently been extended down to ~50.5 Ma and dated using magnetostratigraphic correlations constrained by the U-Pb age of a tuff at 50.0 ± 0.4 Ma (Meijer et al., 2019). An alternative age model has been proposed afterward by F. Yang et al. (2019), but this study did not include the

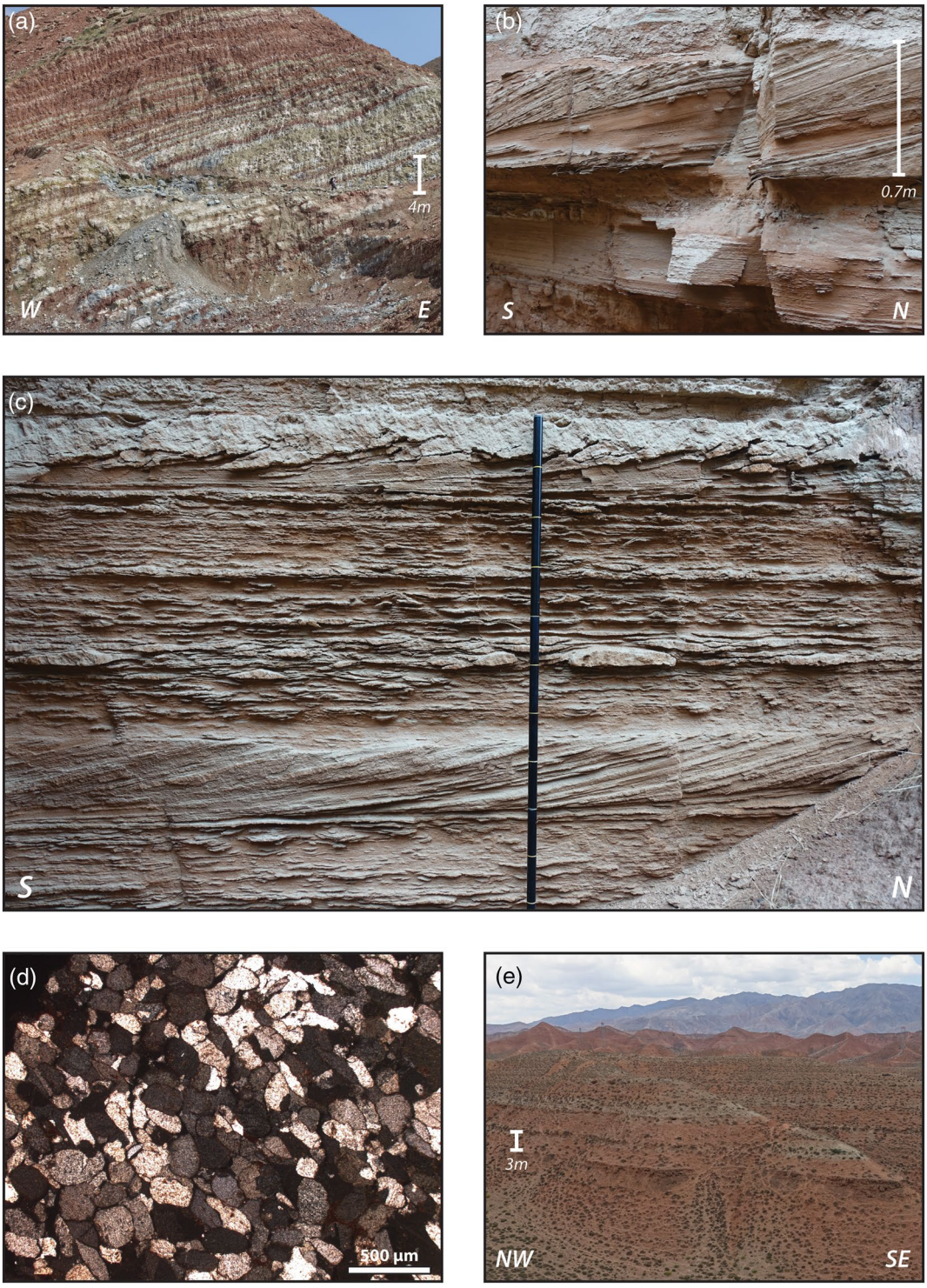

Figure 2. Pictures showing: (a) Cyclic alternations between red mudrocks and gypsum beds at the Xiejia section. (b) and (c) gypsarenites at the Baimasi section showing planar cross-bedding and horizontal bedding interpreted as eolian dunes and sand sheets respectively. (b) is at the 27 m-level and (c) at the 20 m-level with 10 cm markings on the Jacob's staff for scale. (d) thin section under plain-polarized light of the cross-bedded gypsarenite at the 27 m-level of the Baimasi section showing rounded and well-sorted grains of gypsum; (e) top of the Baimasi section showing regular ~3 m alternations between gypsum beds and red mudrocks characteristic of the upper Mahalagou Formation followed by brownish-red mudrocks characteristic of the Xiejia Formation.

Table 1
Locations of Studied Sections

Sections	GPS coordinates	References
Baimasi	36°31'6"N, 102°6'14"E	J. Zhang, Wang, et al. (2016)
Caijia	36°36'55"N, 101°59'03"E	Meijer et al. (2019)
Shuiwan Oligocene profile	36°39'43"N, 101°52'11"E	Abels et al. (2011); Dupont-Nivet et al. (2007)
Tiefo	36°34'37"N, 101°52'50"E	Bosboom et al. (2014)
Xiejia	36°31'20"N, 101°52'20"E	Dai et al. (2006); Dupont-Nivet et al. (2007); Meijer et al. (2019)
Xiejia loess profile	36°31'12"N, 101°52'17"E	This study

radiometric age of the tuff layer and missed several reversed polarity zones in the gypsiferous upper part of the stratigraphy, likely due to a strong normal overprint observed in these beds. It remains unclear to what extent the deposits of the early to middle Eocene are orbitally forced and whether they are formed by the accumulation of eolian dust as observed in the Mahalagou Formation.

3. Materials and Methods

3.1. Sections

We sampled previously described and dated sections (Table 1; Figure 1b) for grain-size analysis and new fossil pollen assemblages to create a composite record covering the early to late Eocene. These sections include the 125 m-thick Tiefo section (Bosboom et al., 2014), and a freshly excavated quarry in the upper 170 m of the Xiejia section (Dupont-Nivet et al., 2007; Meijer et al., 2019), both covering the upper Honggou to lower Mahalagou Formations. We also sampled the previously studied, 275 m-thick Caijia section (Meijer et al., 2019), covering the Qijiachuan to Honggou Formations. This section was sampled for X-Ray Fluorescence (XRF) scanning and color measurements to construct time series for cyclostratigraphic analysis in addition to grain-size analysis and fossil pollen. Detailed methods and sampling resolution of the various analyses follow below. The Baimasi section (J. Zhang, Wang, et al., 2016), was logged using a Jacob's staff and sampled for magnetostratigraphy and grain-size analysis. Additionally, we collected 11 grain-size samples from a 12-m profile of the Oligocene deposits north of the Shuiwan section (Abels et al., 2011; Dupont-Nivet et al., 2007), and 10 grain-size samples from a 1-m loess profile near the Xiejia section for comparison with the Eocene GSDs. This profile consists of loosely packed silt-sized sediments with a massive sedimentary structure and is found at high elevation (2,370 m) indicating an eolian origin (Figure S1). These deposits are therefore interpreted as Quaternary loess following the criteria of Pye (1995).

3.2. Magnetostratigraphy

Paleomagnetic samples were taken at the Baimasi section using a portable electric drill and a compass mounted on an orientation stage at ~1 m resolution where possible resulting in 68 samples. These samples were analyzed in the laboratory of paleo- and rock magnetism at the German Research Centre for Geosciences (GFZ) in Potsdam. After cutting, the samples were thermally demagnetized with increments of 120°C for the first step, followed by increments of 50°C up to 620°C and a final step at 650°C resulting in 12 temperature steps in total. A viscous normal overprint was removed during demagnetization up to 200°C (Figure S2a). Subsequent heating up to 650°C resulted in a linear demagnetization toward the origin (Figure S2a). The thermal demagnetization pattern is similar to previous paleomagnetic studies in the Xining Basin and indicates the dominant magnetic carriers being magnetite, due to a drop in remanent magnetization at ~580°C, and hematite, due to retaining remanent magnetization beyond 650°C (Dai et al., 2006).

3.3. Grain-Size Analysis

Mudrocks of the studied sections were sampled at ~1 m resolution where possible resulting in 442 samples in addition to the 10 sediment samples from the Quaternary loess profile mentioned above. Grain-size

analysis was performed on these samples in the sediment laboratory (Sedlab) of Section 4.6 Geomorphology at the GFZ in Potsdam. Beds of evaporites and carbonates were not sampled. The samples were pretreated in several steps to remove organic matter, carbonate and gypsum and to disperse the grains. To enhance the efficiency of the chemical treatments, the rock samples were first disaggregated using a mortar and pestle, but carefully to make sure no individual grains were broken. Second, ~1 g of sample was used for further treatment and 2.5 ml of 30% hydrogen peroxide (H_2O_2) was added to remove the organic matter. The samples were left to react on a shaking table for at least six days until the reaction stopped. Third, 2.5 ml of 10% hydrochloric acid (HCl) was added and the samples were left on a shaking table for two days to dissolve the carbonate. Fourth, 50 ml of deionized water was added and the samples were left in an overhead shaker for three days to dissolve the gypsum. The deionized water was refreshed every day. Fifth, 0.1 g of sodium pyrophosphate ($Na_4P_2O_7$*$10H_2O$) in a 2.5 ml solution was added and the samples were left in an overhead shaker for at least 12 h to disaggregate the grains.

The samples were measured in suspension using a Horiba Partica LA-950 v2 laser diffraction particle sizer with a reported measurement range of 0.01–2,500 μm and therefore suitable for analyzing mudrocks. The diffraction data were converted to GSDs using the Mie optical model, which is recommended for particle sizes below 30 μm (Varga, Gresina, et al., 2019). However, the Mie model requires the refractive index and the absorption coefficient of the measured particles as input. These are difficult to constrain because the samples are composed of an unknown mix of minerals. Therefore, we tested a wide range of refractive indices (1.4–2.45) and absorption coefficients (0–1) and compared the GSDs (Figure S3). Artificial peaks appear in the submicron-range when the absorption coefficient approaches zero, as is reported in previous studies (Sperazza et al., 2004; Varga, Gresina, et al., 2019). Otherwise, the GSDs are consistent and show only minor variations. Hereafter, we used a refractive index of 1.55 and an absorption coefficient of 1. GSDs are given in 92 size bins logarithmically distributed between 0.011 and 2,500 μm. Some of the measured residues were observed and photographed using an optical microscope to check the reliability of the measurements (Figure S4).

To unmix the GSDs, we used the nonparametric end-member analysis implemented in the AnalySize software package (Paterson & Heslop, 2015). Although this analysis is nonparametric and therefore requires no predefined function of the end-members, the number of end-members needs to be prescribed. Tests with synthetic mixtures have shown that the use of an incorrect number of end-members leads to unreliable results (van Hateren et al., 2018). We ran the analysis using 1 to 10 end-members and found that four end-members are necessary to account for most (98.6%) of the variance in the data set ($R^2 = 0.986$). Increasing the number of end-members does not significantly improve the quality of fit (Figure S5a) and using fewer end-members does not sufficiently cover the entire range of possible grain-sizes, especially below 2 μm (Figure S5b). Furthermore, we found that the end-member interpreted as loess-like and its increase at 40 Ma are robust features of the grain-size record regardless of the predefined number of end-members. The median grain-size, end-member abundances and sample-wise R^2 of the individual sections are shown in Figure S6. A composite grain-size record was created by linear interpolation of the samples between correlated polarity zone boundaries in the various sections.

3.4. Cyclostratigraphy

We constructed time series of the Caijia section by measuring XRF scanning and color at 0.5 m resolution resulting in 515 samples in total. The samples were carefully ground, assembled in 32 mm cups, covered by a 4 μm polypropylene film and measured using an ITRAX XRF core scanner. XRF intensities (in counts per second) were obtained for the 13 elements Al, Si, S, Cl, K, Ca, Ti, V, Mn, Fe, Rb, Sr, and Zr. All statistical analyses were performed on element intensity records after log-ratio or centered-log-ratio transformation. We used principal component (PC) analysis as implemented in the ItraXelerate software (Weltje et al., 2015) to examine the covariance between the individual elements in our data set. The results are presented in a biplot of PC1 and 2, which reveals three groups of elements (Figure S7). Lithogenic elements (Fe, Ti, K, Si, Al, and Rb) are positively correlated and clearly separated from the authigenic elements (Ca, S, and Sr) by PC1, which explains 72.7% of the variance. The authigenic elements can be subsequently separated into carbonates (Ca) and gypsum (S and Sr) along PC2 explaining another 12.7% of the variance. We construct time series by using the dominant elements of these three groups (Ti, Ca, and S). Hence, relative varia-

tions of lithogenics, carbonates and gypsum are represented by log-ratios of Ti/Ca, S/Ti and S/Ca, which provide the most easily interpretable signals of relative changes in the chemical composition (Weltje & Tjallingii, 2008).

RGB-values were extracted from high-resolution photographs produced by the corescanner to construct a color record. The average values of 10 representative pixels were used and converted to CIELAB color space for interpretation purposes. These values include: L* (lightness), a* (red over green), and b* (yellow over blue). However, note that these values are not calibrated and should only be used to study relative changes throughout our record. Spectral analysis was performed using Redfit (Schulz & Mudelsee, 2002) as implemented in the Past software (Hammer et al., 2001) with no segmentation, no oversampling and a Welch window. The time series were bandpass filtered using the AnalySeries software (Paillard et al., 1996).

3.5. Palynology

Productive palynological (pollen and spore) samples were collected from gypsum beds and laminated mudrocks in the Tiefo, Xiejia and Caijia sections. Samples collected from red beds in these sections were barren of palynomorphs. The samples were prepared by Palynological Laboratory Services (Anglesey, UK) using standard palynological techniques (HCL, HF, sieving at 10 μm) and examined at the University of Amsterdam, The Netherlands. Ten samples were productive; nine from the Mahalagou Formation, but only one from the Honggou Formation. These samples were added to the previously studied palynological record of the Xining Basin (Bosboom et al., 2014; Dupont-Nivet, Hoorn, & Konert, 2008; Hoorn et al., 2012; Page et al., 2019 and Figure S8). Samples were published as supplementary data for a recent review of Asian steppe ecology (Barbolini et al., 2020) but are first described here for climatic reconstructions of our studied sections. Palynomorphs were identified using the Genera File of Fossil Pollen and Spores (Jansonius & Hills, 1976 and recent updates), Z. C. Song et al. (1999) and the Chinese palynological literature. Plant Functional Types (PFTs) were assigned using the Nearest Living Relatives (NLR) approach applied by Hoorn et al. (2012).

4. Baimasi Section

The late Eocene deposits in the Xining Basin are characterized by mudrocks alternated with gypsum beds (Figure 2a) formed in saline lakes as recognized by previous studies (Abels et al., 2011; Bosboom et al., 2014; Dupont-Nivet et al., 2007). The newly studied Baimasi section is located on the eastern margin of these saline lake deposits and is described in the following. The section is subsequently dated and correlated to the other sections by using magnetostratigraphy and marker beds.

4.1. Lithostratigraphy

4.1.1. Observations

The lithostratigraphy of the Baimasi section consists of red gypsiferous mudrocks and gypsarenites (Figures 2b and 2c). The mudrocks have a horizontally laminated or massive structure. The gypsarenites are horizontally bedded and contain dm-scale sets of planar cross-bedding and laterally extensive horizontal bounding surfaces (Figures 2b and 2c). The foresets have a tangential base and a maximum dip of ∼20°. Measured paleocurrent directions are to the south (Table 2; Figure 3). The gypsarenites are well-sorted and consist of rounded to well-rounded grains of gypsum (Figure 2d). Rare cm-scale beds of very fine sandstone containing ripple and coarse siltstones containing climbing ripple cross-lamination are observed at the ∼30 m-level. Dm-scale beds of green horizontally laminated gypsum are observed at the base and the top of the section and can be correlated to saline lake deposits in the center of the basin. Regular ∼3 m alternations between red mudrocks and gypsum beds are observed on top of the section, followed by a shift to brownish-red mudrocks (Figure 2e).

Table 2
Paleocurrent Directions of Eolian Gypsarenites From the Baimasi Section

Stratigraphic position (m)	Paleocurrent direction azimuth (°)	Direction corrected for tectonic rotation (°)
20.4	180	160
22.2	170	150
27.0	192	172
50.0	130	110

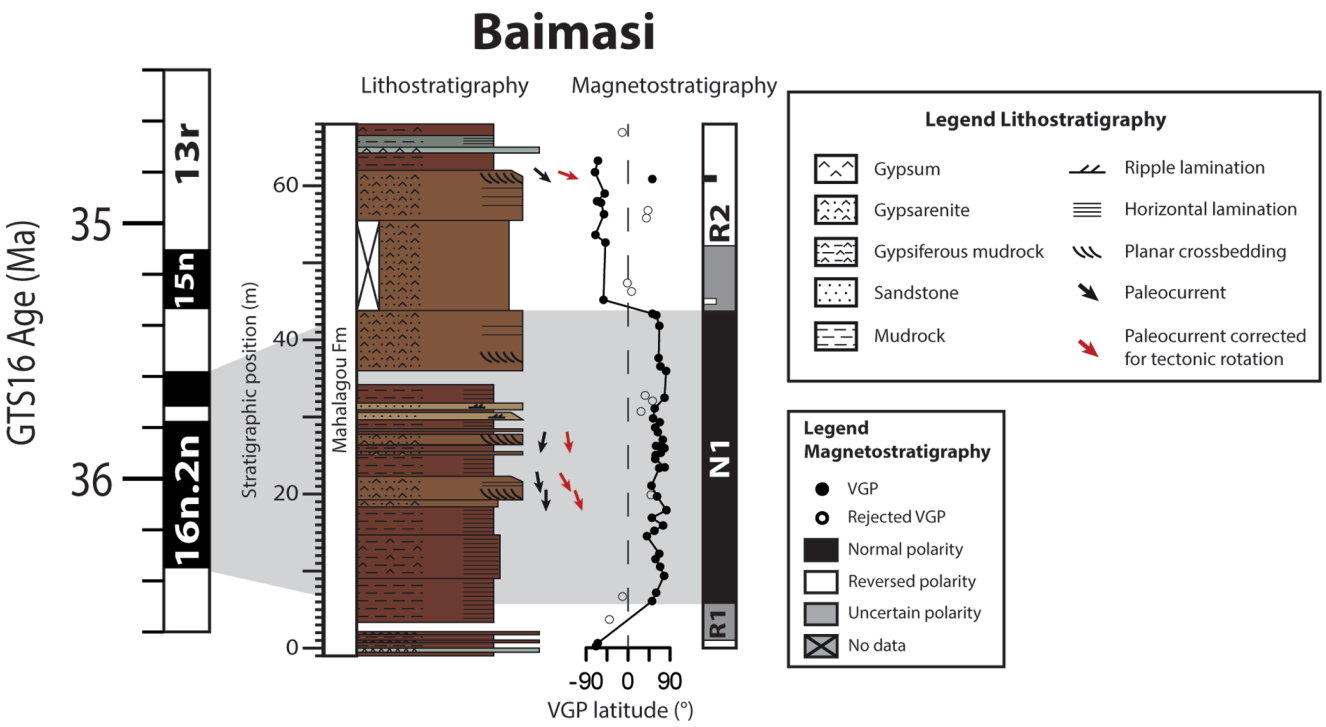

Figure 3. Litho- and magnetostratigraphy of the Baimasi section.

4.1.2. Interpretations

The depositional environment of the gypsiferous mudrocks is interpreted as a dry mudflat and as a saline lake for the gypsum beds (Abels et al., 2011; Dupont-Nivet et al., 2007; Smoot & Lowenstein, 1991; Talbot et al., 1994). The siltstone beds with climbing ripples suggest rapid deposition by unconfined fluvial flows (North & Davidson, 2012). Gypsarenites are rare and almost always associated with eolian transport of gypsum grains deflated from nearby salt pans (Smoot & Lowenstein, 1991). This is corroborated by the rounding and sorting of the gypsum grains and the cross-bedded gypsarenites are thus interpreted as eolian dunes following J. Zhang, Wang, et al. (2016). The horizontally bedded gypsarenites are interpreted as eolian sand sheets. However, we note that the cross-beds observed here are thin with gentler foresets than is common for eolian sands (e.g., McKee, 1966). We argue that is may be due to the low accumulation rates observed in the Xining Basin (~3 cm/kyrs; Abels et al., 2011; Meijer et al., 2019) resulting in only the more gently steeping base of the dunes being preserved.

The measured paleocurrent directions of the gypsarenites are corrected (red arrows in Figure 3) for the clockwise 20° vertical axis rotation of the Xining Basin during the late Paleogene as reported in previous paleomagnetic studies (Dupont-Nivet, Dai, et al., 2008). Although only four beds of cross-bedding are preserved, the paleocurrent directions of these beds are consistently to the south and southeast. This suggests that north to northwesterly winds occurred during the Eocene, which would be similar to the winter monsoons dominating the region northeast of the present-day Xining Basin (Figure 1). However, we note that the Eocene wind directions may be affected by local topography which is poorly constrained.

4.2. Magnetostratigraphy

4.2.1. ChRM Directions

The Characteristic Remanent Magnetization (ChRM) directions were calculated using eigenvector principal component analysis (Kirschvink, 1980) on at least four temperature steps. The resulting directions reveal two clusters of either normal or reversed polarity (Figure S2b). The means of

these clusters were calculated using Fisher statistics (Fisher, 1953) and samples with an angle of more than 45° from the mean were rejected from further analysis (open symbols in Figure 3). The reversals test was performed using the means of the two clusters (McFadden & McElhinny, 1990), but failed due to an unresolved normal overprint as observed in previous studies in the Xining Basin (Dupont-Nivet, Dai, et al., 2008; Meijer et al., 2019). This would make our data set unsuitable for rotational analysis, but does not affect the reliability of the magnetostratigraphy. The Virtual Geomagnetic Poles were calculated and polarity zones are defined on at least two successive samples with the same polarity.

4.2.2. Correlation to the GTS

The Baimasi section contains a reversed polarity zone at the base (R1), followed by a ~40 m-thick normal polarity zone (N1) and a ~20 m-thick reversed polarity zone at the top (R2). The Baimasi section is mapped as the Mahalagou Formation (Dai et al., 2006: QBGMR, 1985 and Figure 1a) and is observed to grade upwards into the brownish-red mudrocks of the Xiejia Formation (Figure 2e). Furthermore, the characteristic meter-scale gypsum beds of the Mahalagou Formation are observed both at the top and base of the section (Figures 2e and 3). These observations confidently constrain the age of the Baimasi section to the Mahalagou Formation, which serves as a starting point for our magnetostratigraphic correlations. The chrons observed in the Mahalagou Formation include: C13 to C18 (Figure 4; Abels et al., 2011). The only long reversed chron in this interval is C13r and we therefore correlate it to R2. C13r is preceded by a short normal and reversed chron (C15n and C15r), which are not observed in the Baimasi section, possibly because this interval is poorly exposed (Figures 3 and 4). Below C15r is a long normal chron, C16n, which we correlate to N1 and R1 is correlated to C16r. This suggests the Baimasi section covers the 36.5–35 Ma interval but our interpretation is limited by the missing reversals of C15n and C15r. Nevertheless, we argue that based on the lithological observations listed above, we can confidently correlate the Baimasi section to the Mahalagou Formation spanning from 40 to 34 Ma.

5. Grain-Size Analysis

5.1. Grain-Size Distributions

The GSDs of the studied sections are dominated by fine silt with a median grain-size of 4–6 μm (Figure 5a). The GSDs measured in this study differ from the late Eocene grain-size record from the Xining Basin reported in Licht et al. (2014), which are characterized by bimodal distributions with modes at 16–31 μm and at 1.6–2.8 μm. The samples in both studies were prepared using similar pretreatments, but measured using a different laser diffraction device. Comparison studies have shown that although laser diffraction measurements are precise and highly reproducible (Goossens, 2008), their accuracy is limited and using different devices may result in different GSDs (Varga, Gresina, et al., 2019). Therefore, care should be taken when comparing GSDs between studies and we thus exclude the results of Licht et al. (2014) in this study. The comparison with the GSD of Quaternary loess (Figure 5b) is made with samples measured using the same pretreatment, laser diffraction device and optical settings.

5.2. End-Member Analysis

End-member analysis of the data set reveals four end-members (Figure 5a) based on the best correlation (R^2) per grain-size class. Three of these end-members have modes at 2.6 μm (EM1), 5.1 μm (EM2), and 10.1 μm (EM3). A fourth end-member is fine skewed with a mode at 51.5 μm (EM4). The composite record (Figure 6) shows that the lower part of the stratigraphy (50.5–40 Ma) is dominated by EM1, EM2, and EM3, while the abundance of EM4 is low (5% on average). The upper part of the record (40-36 Ma) is dominated by EM3 and EM4, while the abundance of EM1 and especially of EM2 are reduced. At 40 Ma, the abundance of EM4 increases abruptly to an average of 19% in different sections (Tiefo and Xiejia) at the same stratigraphic level suggesting a laterally continuous shift (Figure S6), coeval with the previously recognized onset of obliquity cycles and increase in steppe-desert pollen (Bosboom et al., 2014). Samples from the Oligocene mudrocks show similar end-member abundances as in the upper part of the Eocene record (Figure S6).

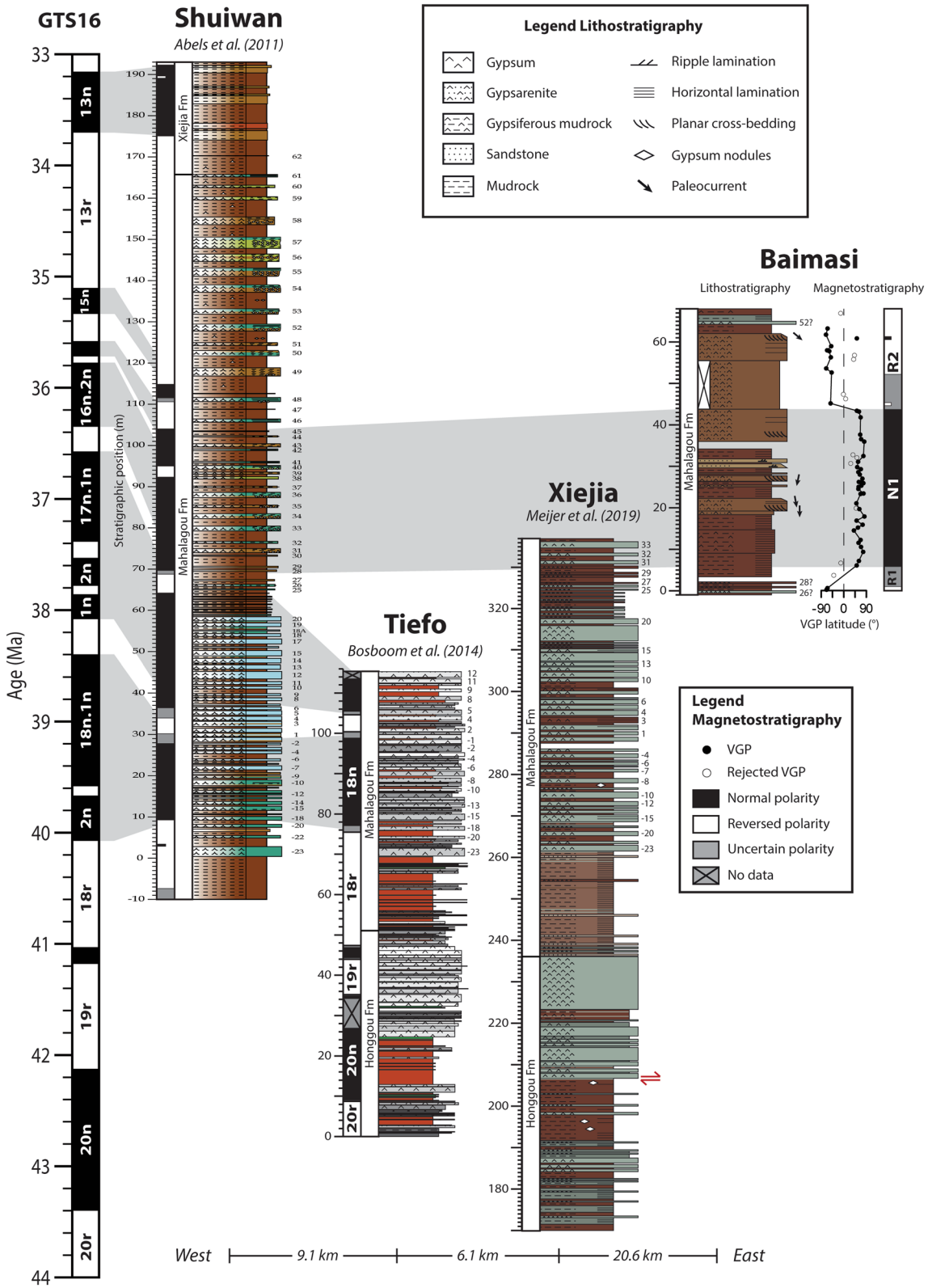

Figure 4. Lithostratigraphic and magnetostratigraphic correlations between the Shuiwan (Abels et al., 2011), Tiefo (Bosboom et al., 2014), Xiejia (Meijer et al., 2019) and Baimasi sections and the GTS16 (Ogg et al., 2016).

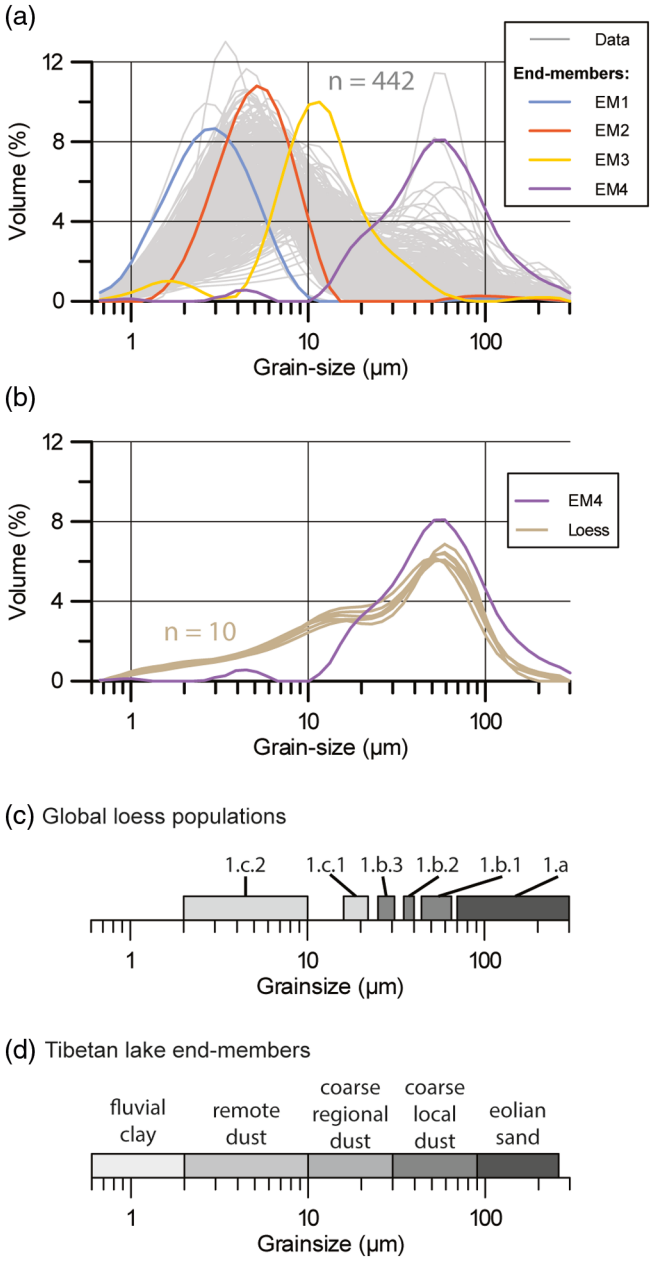

Figure 5. (a) Frequency curves of the total measured GSDs and of the end-members. (b) Comparison of EM4 with the GSD of local Quaternary loess in the Xining Basin. (c) Size ranges of global loess populations identified by Vandenberge (2013). (d) Size ranges of end-members in Tibetan lake records (Dietze et al., 2014). GSD, grain-size distribution.

5.3. End-Member Interpretations

The GSD of EM4 is remarkably similar to the Quaternary loess in the Xining Basin (Figure 5b), which corresponds to the coarse local dust component observed in global loess populations (1.b.1 in Vandenberghe, 2013, Figure 5c) and in Tibetan lake deposits (Dietze et al., 2014, Figure 5d). However, it should be noted that the GSDs of loess may vary considerably depending on the source and distance to the source (e.g., Pye, 1995; Újvári et al., 2016; Vandenberghe, 2013). Furthermore, similar GSDs are observed on mudflats formed by fluvial transport (van Toorenenburg et al., 2018) and therefore the GSD alone is not a diagnostic feature for eolian transport. Additional evidence is provided by the U-Pb age spectra of detrital zircon grains indicating a provenance for the silt-sized fraction (10–45 μm) different from Eocene fluvial deposits but similar to Quaternary loess (Licht et al., 2016). Furthermore, previous surface morphology analyses of the >20 μm quartz grains identified features such as dish-shaped depressions and adhering clay particles, which suggest a prolonged eolian transport for these grains (Licht et al., 2014). However, it should be noted that it remains unclear whether these features are formed by the eolian transport of silt-sized grains or are inherited from older phases of eolian transport (e.g., Krinsley & McCoy, 1977). Lastly, the abrupt, laterally continuous increase of EM4 suggests an eolian rather than a fluvial origin linked to local dynamics. Cross-bedded silt- and sandstone beds indicating fluvial transport are observed as well, but decrease upwards (Meijer et al., 2019). Such channels only reappear during the Miocene related to the uplift of the nearby mountain ranges (G. Xiao et al., 2012; R. Yang et al., 2017), while there is no evidence of a tectonic event at 40 Ma. This suggests a reduction in fluvial activity rather than an increase at 40 Ma as observed in EM4. We note that the observations listed above, when considered on their own, are not strictly diagnostic of windblown transport (Meijer et al., 2020), but argue that when taken together, these observations suggest an eolian origin as the most likely. We therefore interpret the increase of EM4 as the onset of a loess-like dust component, which remains a consistent part of the sedimentary record afterward.

The finer-grained end-members may occur in several sedimentological settings and their origin is more difficult to assess because these grains are too small for single-grain provenance and quartz surface morphology analyses. In terms of eolian dust, these end-members may occur as long-term suspension transport, possibly by upper-level westerlies (Pye, 1995; J. Sun, 2002), or as aggregates in short-term suspension as observed in modern-day dust storms (M. Qiang et al., 2010). We also note that EM3 might reflect the fine-grained dust component commonly observed in the Mio-Pliocene records of the Red Clay Formation (Shang et al., 2016). Alternatively, a fluvio-lacustrine origin may be inferred either in suspended load or as mud aggregates transported in bedload (Wright & Marriott, 2007). Because of these difficulties, we refrain from deriving any sedimentological and paleoclimatic information using these end-members and focus on EM4 instead. Note, that because we only interpret EM4 with an average abundance of 19% as being eolian in origin, the Xining deposits are not predominantly composed of windblown silt in contrast to previous interpretations (Licht et al., 2014, 2016). Therefore, these deposits are not classified as lithified loess (Pye, 1995), but rather interpreted as a diverse depositional environment containing a loess-like component as well as other fluvio-lacustrine and/or dust components (Figure 7). This interpretation is in line with recent depositional models for the Miocene Red Clay (Alonso-Zarza et al., 2009; Liu et al., 2019; Meijer et al., 2020).

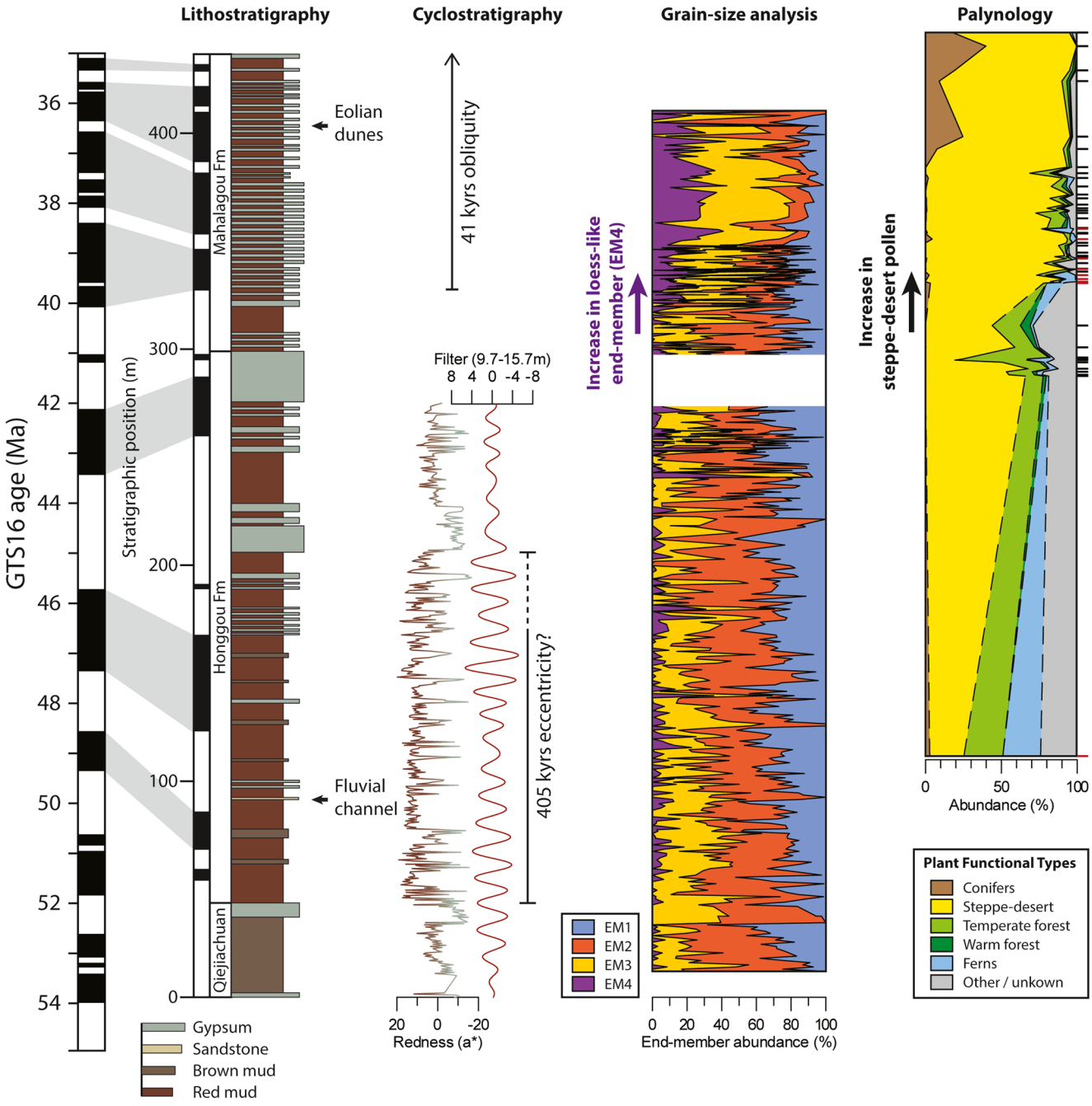

Figure 6. Composite of the early late Eocene record of the Xining Basin based on magnetostratigraphic correlations between the studied sections. The composite shows the lithostratigraphy, cyclostratigraphy and end-member abundances of the grain-size record and Plant Functional Type abundances of the palynological record with new samples from this study and Barbolini et al. (2020) indicated in red. The magnetostratigraphy is correlated to the GTS16 (Ogg et al., 2016). Note that the increase in the loess-like end-member (EM4) at 40 Ma is coeval with the onset of 41 kyr obliquity cycles and the increase in steppe-desert pollen previously recognized by Bosboom et al. (2014).

6. Cyclostratigraphy

The increase of loess-like dust at 40 Ma is coeval with the onset of obliquity cycles in the Xining Basin previously recognized by Bosboom et al. (2014) in the middle-late Eocene records. In the following, we perform time series analysis on the Caijia section, which covers the Qijiachuan and Honggou Formations, to examine whether the record in the Xining Basin is orbitally forced in the early to middle Eocene.

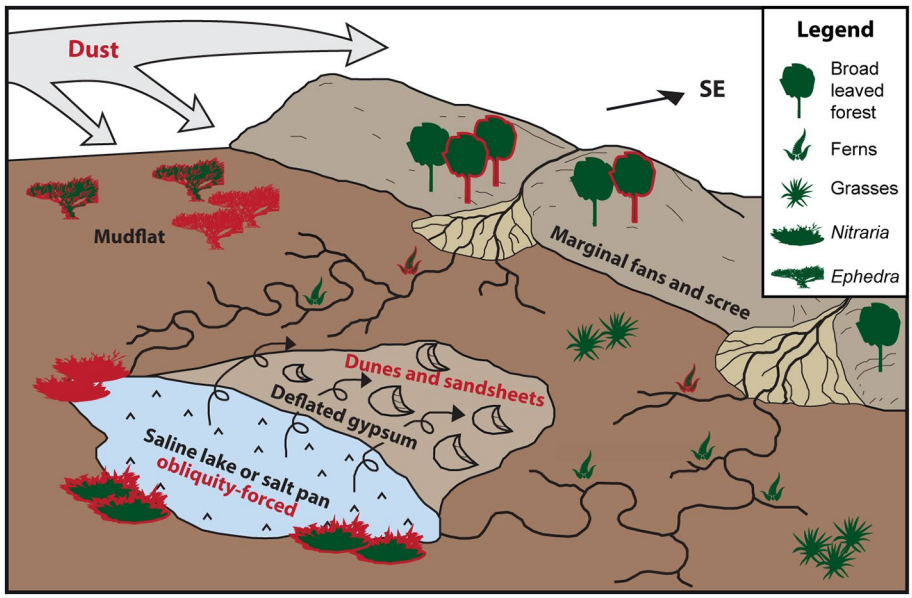

Figure 7. Depositional environment and paleovegetation of the Xining Basin during the Eocene (modified from Meijer et al., 2020). Dominant vegetation before 40 Ma is indicated in green, and after 40 Ma, in red (vegetation present throughout is colored in green with red outline). Sedimentary features appearing after 40 Ma are also indicated in red.

6.1. Cyclicity

The Honggou Formation is dominated by massive brick-red mudrocks, similar to the overlying Mahalagou Formation and interpreted as a dry mudflat (Figure 8; Meijer et al., 2019). The red mudrocks are alternated with meter-scale intervals of brown to green mudrocks with fine horizontal laminations interbedded with cm-scale beds of carbonate and gypsum. These laminated mudrocks are interpreted as lacustrine and reflect wetter atmospheric conditions (Figure 8; Meijer et al., 2019). The alternations between the red and lacustrine mudrocks are regular, but with a long period of 10–12 m compared to the meter-scale cycles in the overlying Mahalagou Formation. Thirteen of these low frequency cycles can be identified in the Caijia section (Figure 8). No lacustrine deposits are identified in cycle 4 (Figure 8), but a meter-scale channel body of very fine sandstone is observed here instead. The channel body contains trough cross-bedding and grades laterally into cm-scale beds of very fine sandstone with ripple laminations interpreted as fluvial deposits (Meijer et al., 2019). Two of the cycles contain gypsum beds instead of lacustrine mudrocks (cycle 5 and 8; Figure 8) indicating more saline conditions (Meijer et al., 2019). Gypsum beds are more common in the upper part of the Honggou Formation and the cyclicity is less obvious. Two groups of meter-scale gypsum beds with a lacustrine interval in between may represent three more cycles (cycle 11–13; Figure 8). Afterward, no more cycles are observed in the upper part of the section. No cyclicity is observed as well in the Qijiachuan Formation at the base.

6.2. Spectral Analysis

Spectral analysis (Figure 8) of the color records reveals a >95% confidence peak at a period of 12 m in a* (red over green) and b* (yellow over blue). L* (lightness) shows a >99% confidence peak at 19.6 m. The bandpass filter of L* shows that this period follows the occurrence of gypsum and carbonate beds, but fails to identify some of the lacustrine mudrocks which have a similar lightness as the red mudrocks. Therefore, the 19.6 m period may represent a double cycle of the 12-m cyclicity. The XRF proxies Ca/Ti and S/Ti are dominated by higher frequency cycles with periods of 1–3 m, which reflect the individual gypsum and carbonate beds that occur in the lacustrine intervals, but lack the lower frequency cycles observed in the color records. The lower frequency cycles are represented in the Ca/S record which shows a >95% confidence peak at 10.6 m (Figure 8). No cyclicity is observed in the grain-size record, which is discussed below.

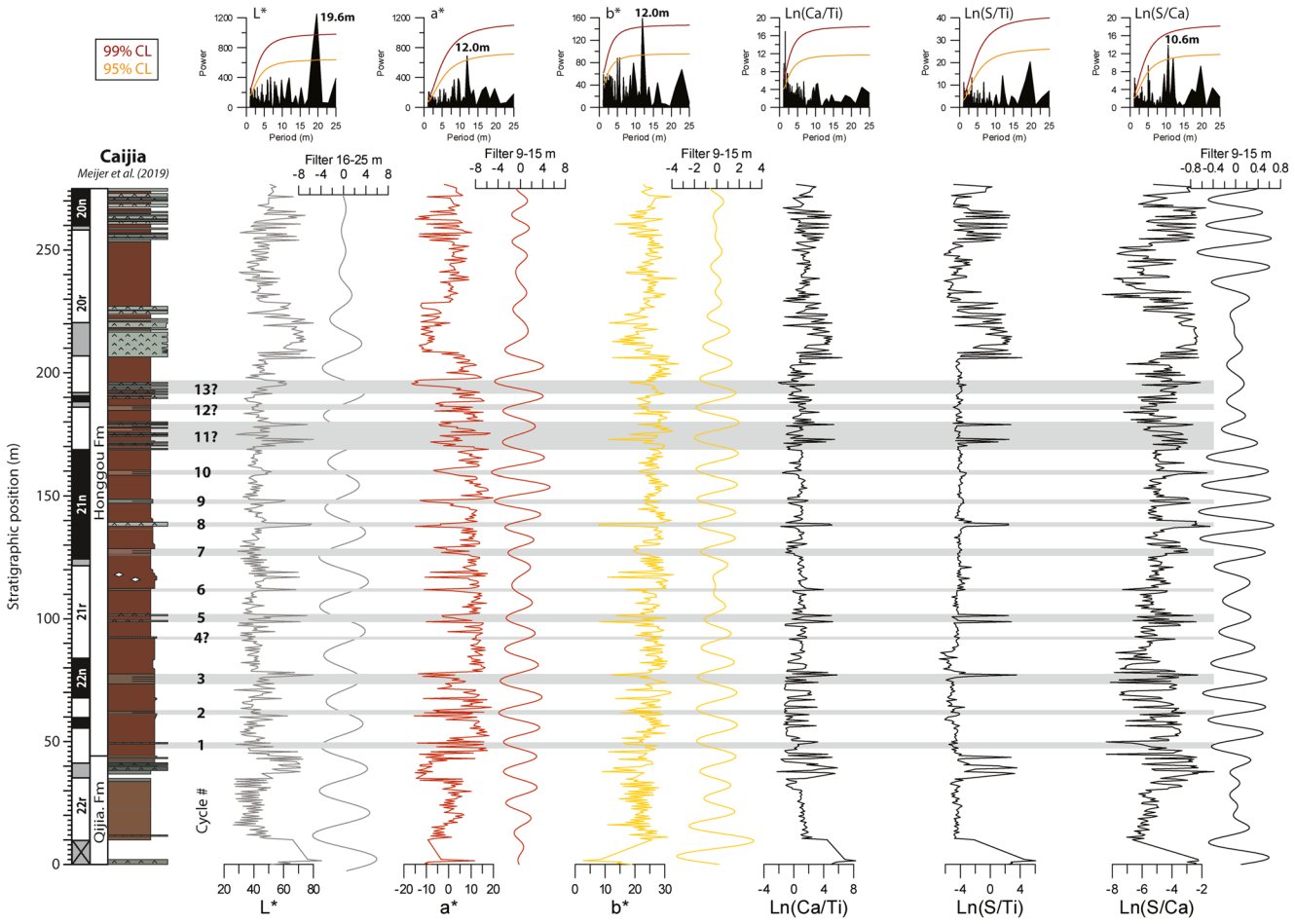

Figure 8. Time series of the Caijia section showing the color records: L* (lightness), a* (red over green) and b* (yellow over blue) and XRF record of log-ratios: Ca/Ti, S/Ti and Ca/S. Redfit spectral analyses with confidence limits (CL) are shown above and the bandpass filters using the dominant period of the individual records are shown on the right. The cycles are numbered and the wet phases represented by lacustrine mudrocks, gypsum beds and fluvial sandstones are marked in gray. Litho- and magnetostratigraphy is from Meijer et al. (2019). XRF, X-Ray Fluorescence.

6.3. Correlations

The cycles in the 50-45 Ma interval of the Caijia section can be correlated bed-to-bed to the East Xining section located ~9 km to the west (Figure S9). Similar cycles are observed as well in the Xiejia section, located ~14 km to the south. However, these cycles consist of sandstone beds in the lower part instead of lacustrine mudrocks (Figure S9). The Xiejia section is located in a more proximal setting toward the southern margin of the basin which may explain the occurrence of fluvial sandstones during the wet phase of the cycles. Similar orbital cycles are observed in the mudflat deposits of the Teruel Basin in Spain with distal lacustrine deposits correlating to proximal fluvial beds during the wetter phases (Ventra et al., 2018). The correlations in the Xining Basin suggest that the cycles are basin-wide and possibly orbitally forced. The accumulation rates are relatively constant at 3 cm/kyrs for the Honggou Formation (Meijer et al., 2019), which suggests that the cycles of 10–12 m have a duration of 333–400 kyrs and may be forced by the long eccentricity cycle of 405 kyrs. To identify possible phase relations and driving mechanisms of the Caijia sedimentary record, we correlated the record with various astronomical solutions (Laskar et al., 2011, Figure 9). The sedimentary cycles are dated using the magnetostratigraphy of (Meijer et al., 2019) and various age models for the chron boundaries (Gradstein et al., 2012; Westerhold et al., 2015; 2017 and Figure 9). The most recently tuned age model (Westerhold et al., 2017) reveals that the wet phases of the cycles correlate to the 405-kyrs eccentricity minima in the astronomical solution (Laskar et al., 2011, Figure 9).

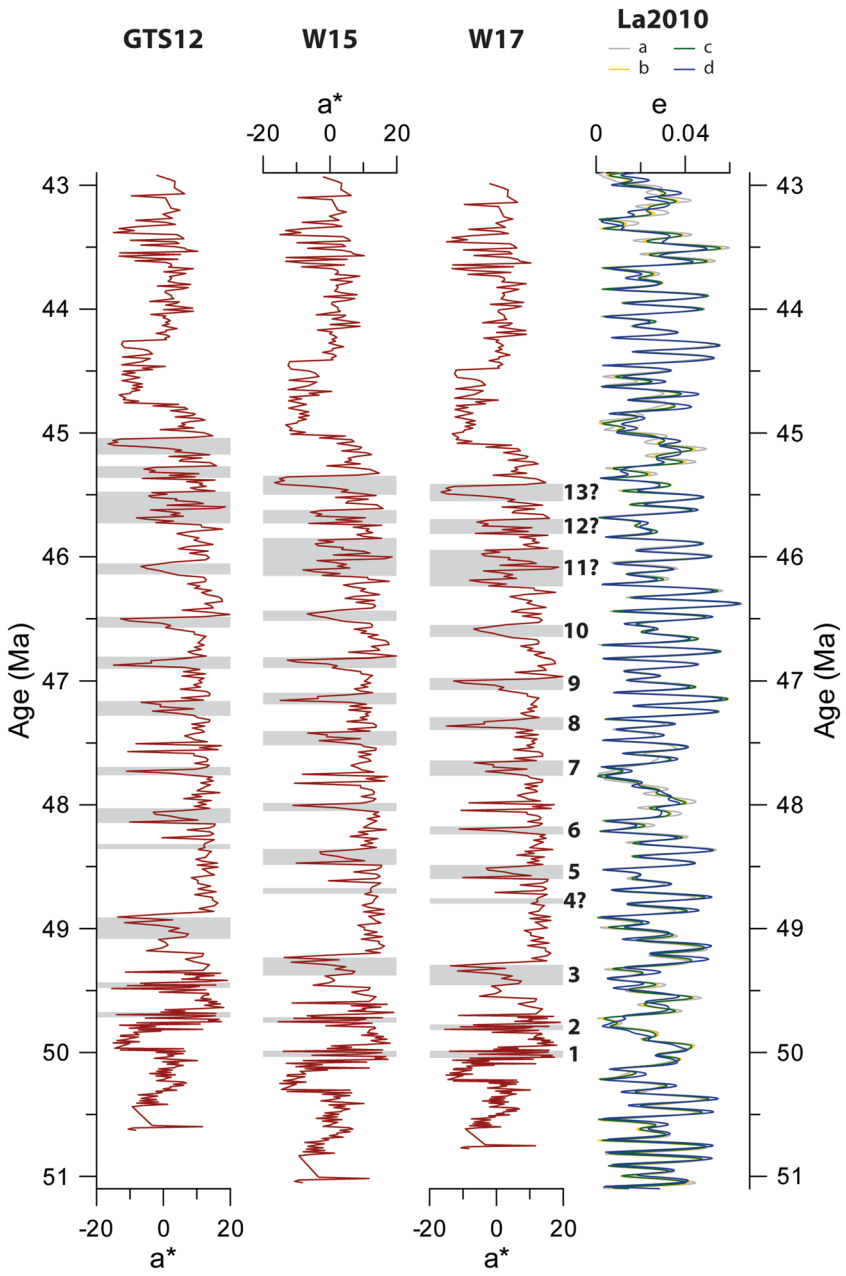

Figure 9. Color record a* (red over green) of the Caijia section correlated to the astronomical solutions (a–d) of eccentricity, e (Laskar et al., 2011). The ages of the Caijia section are calculated by linear interpolation between chron boundaries identified by (Meijer et al., 2019). The base of the Caijia section is correlated to the top of C23n. Chron ages of the following timescales are used: GTS12 (Gradstein et al., 2012), W15 (Westerhold et al., 2015) and W17 (Westerhold et al., 2017). W17 shows wet phases of cycle 1 to 13 during 405-kyr eccentricity minima.

6.4. Interpretations

In the following, we explore the occurrence of the ~400-kyr cycles in terms of orbital forcing. Climate model simulations testing the role of orbital forcing under modern-day boundary conditions suggest that both the summer monsoons and wintertime westerlies are driven directly by orbital forcing through Northern Hemisphere insolation, although the phase is opposite (Bosmans et al., 2018; Shi et al., 2011; X. Zhang, Jin, et al., 2016). At the midlatitudes, this insolation is dominated by the precession cycle and, to a minor

extent, by the obliquity cycle. The 405-kyr eccentricity cycle is only a modulation of the shorter precession and 100-kyr eccentricity cycles and therefore, the lack of these higher frequency cycles in our record is puzzling. Other studies have identified similar low frequency cyclicities in the absence of higher frequency cycles and ascribed this to limitations of the paleoenvironmental record in preserving the higher frequency cycles (Abels et al., 2010) or to a clipped insolation response resulting in only the most extreme amplitudes being recorded (Nie et al., 2008). Alternatively, the paleoenvironmental response to orbital forcing may be modulated by other mechanisms. Marine records show that the lower frequency cycles such as the 405-kyr eccentricity cycle are preferentially amplified in the carbon cycle during the Cenozoic (Kocken et al., 2019) and therefore may have affected the Xining Basin via CO_2 forcing. Additionally, teleconnections with the Antarctic ice sheets are proposed for the occurrence of 100-kyr eccentricity cycles in various Miocene records across the northeastern Tibetan Plateau (Z. Wang et al., 2019) and the incipient Eocene ice sheets may have similarly modulated the paleoenvironment in the Xining Basin. Regardless of the explanation for the 400-kyr cycles, our cyclostratigraphic analysis reveals no higher frequency cycles in the record before 40 Ma, even though the sampling resolution of ∼0.5 m corresponds to ∼17 kyrs (based on the average accumulation rate of 3 cm/kyr from Meijer et al., 2019) and should be enough to detect obliquity and 100-kyr eccentricity cyclicities. In addition, no cycles at all are identified in the record between 45 and 40 Ma. This is in stark contrast to the obliquity cycles observed after 40 Ma by previous studies (Abels et al., 2011; Bosboom et al., 2014; Dupont-Nivet et al., 2007; Huang & Hinnov, 2019; G. Q. Xiao et al., 2010) suggesting a major paleoenvironmental shift at this time.

7. Palynology

To study the vegetation response to the 40 Ma event, we complement the existing palynological record of the Xining Basin withsamples from the early and middle Eocene (Figure 6). Only one sample from the early Eocene was productive and reveals a semi-arid steppe-forest ecosystem occupied by xerophytic grasses and halophytic shrubs (*Graminidites* and *Nitraria* respectively), that also hosted considerable areas of temperate woodland and ferns surrounding watercourses (Figure 7). The middle Eocene is represented by multiple samples indicating a more arid steppe-desert environment than the early Eocene, with a now-subordinate component of temperate broad leaved forest. This is followed by a major increase in both the abundance and diversity of the xerophytic and halophytic desert and steppe shrubs, *Ephedra* and *Nitraria*, and a concurrent decrease in temperate broad-leaved forest diversity. After this shift, steppe-desert vegetation (alternating between *Ephedra* and *Nitraria* being dominant) comprises around three-quarters or more of the palynological assemblage, with many samples including 80–95% steppe-desert pollen. This reflects a significant drying event previously recognized by Bosboom et al. (2014) and now better constrained by our pollen samples to occur between 40.7 and 39.9 Ma. This shift is again coeval with the onset of obliquity cycles (Bosboom et al., 2014) as well as the appearance of the loess-like end-member observed in our grain-size analyses (Figure 6). The late Eocene record is characterized by the appearance of conifers at ∼37 Ma, as recognized in previous studies, and linked to cooling and aridification (Abels et al., 2011; Barbolini et al., 2020; Dupont-Nivet, Hoorn, & Konert, 2008; Page et al., 2019).

8. Discussion

Our study shows an abrupt shift occurring in the Xining Basin with the appearance of a loess contribution (EM4) at 40 Ma (Figure 6), coeval with the onset of obliquity-forced moisture cycles and a large increase in the proportional abundance of steppe-desert pollen previously recognized by Bosboom et al. (2014). Although the latter likely indicates a marked expansion of low-growing, bushy shrubs that would have acted as efficient local dust traps (Pye, 1995), the vegetation shift alone cannot explain the onset of dust in the basin because these taxa were also relatively abundant at intervals prior to 40 Ma (Figure 6). Furthermore, these sudden changes are unlikely to be related to the slow local tectonics occurring in the Xining Basin at this time (L. G. Fan et al., 2019), but rather imply a regional reconfiguration of the atmospheric circulation.

8.1. Onset of the Siberian High

Modern-day observations show that the northwesterly winter monsoons are driven by the Siberian High resulting in dust storms due to the break-up of this high-pressure system during spring (Roe, 2009). Therefore, the appearance of both the dust in the grain-size record and the prevailing northwesterly winds evidenced in the Baimasi section may indicate the establishment of a similar atmospheric configuration at 40 Ma. This is corroborated by provenance data showing that the source of the Xining dust was identical to the Quaternary loess suggesting that the Asian atmospheric circulation has been a resilient feature since the late Eocene (Licht et al., 2016). The establishment of the Siberian High would also explain the cyclicity appearing at 40 Ma, because this high-latitude pressure system is primarily driven by changes in insolation related to obliquity at orbital timescales (Shi et al., 2011) and interacts with atmospheric moisture from the monsoons and westerlies. A stronger Siberian High during high obliquity deflects more atmospheric moisture, whereas low obliquity results in a weaker high-pressure system and more moisture transported inland. During the Eocene, the Xining Basin is proposed to have been dominated by moisture derived from the wintertime westerlies (Meijer et al., 2019) and therefore would have been especially susceptible to the Siberian High. Overall, the presence of the Siberian High would have enhanced the aridification of the region and driven the shift to widespread steppe-desert vegetation. We thus propose that the changes observed at 40 Ma could mark the onset of atmospheric circulation associated with the establishment of a high-pressure system developing over Siberia. While some climate model simulations using Paleogene boundary conditions suggest the onset of a proto-Siberian High as early as the late Paleocene with wind directions in agreement with our observations (Farnsworth et al., 2019), others suggest an absence of the Siberian High until at least the middle Eocene due to the warmer Eocene winter temperatures (Tardif et al., 2020). Instead, these simulations show a belt of high atmospheric pressures between 20 and 45°N during winter with dominant surface wind directions in the Xining Basin toward the east (Tardif et al., 2020) or northeast (Huber & Goldner, 2012). These ambivalent results may reflect variations in internal model properties representing winter conditions, and other boundaries conditions that may have driven the onset of the Siberian High: Paleogene atmospheric cooling, Tibetan Plateau uplift and proto-Paratethys Sea retreat all occurring during this time window. In the following, we consider the respective contributions of these proposed driving mechanisms.

8.2. Driving Mechanisms

In a first-order view atmospheric cooling is proposed to drive aridification (Dupont-Nivet et al., 2007; Lu et al., 2010) and expand Arctic sea ice strengthening the Siberian High (Roe, 2009). Global temperatures dropped during the Eocene starting at 50 Ma (Cramwinckel et al., 2018) and ephemeral sea ice in the Barents Sea is recorded since at least 45 Ma (Tripati & Darby, 2018), both predating the 40 Ma event in the Xining Basin. Furthermore, a recent study using clumped isotopes to reconstruct atmospheric temperatures in the Xining Basin found no cooling event at 40 Ma, but rather a two-tiered cooling at 37 Ma and at the Eocene-Oligocene Transition (EOT), 33.5 Ma (Page et al., 2019). Both cooling steps are interpreted to correlate with aridification events identified as a decrease in gypsum beds (Abels et al., 2011; Dupont-Nivet et al., 2007) and a decrease in reconstructed soil water $\delta^{18}O$ (Licht et al., 2020). However, we do not observe an increase in the loess-like end-member at 37 Ma (Figure 6), nor in the Oligocene deposits after 34 Ma (Figure S6), even though atmospheric cooling is expected to intensify the Siberian High. It seems that a threshold has been crossed previously at 40 Ma and subsequent changes did not significantly enhance dust deposition in the Xining Basin.

Climate model sensitivity simulations suggest that the winter monsoons and Siberian High are sensitive to uplift of the Tibetan and the Mongolian Plateau (Sha et al., 2015; Yu et al., 2018; C. Zhu et al., 2019). Uplift of the latter is poorly constrained to be late Cenozoic (Vassallo et al., 2007) and therefore postdates the onset of dust in the Xining Basin. In contrast, numerous studies report that the Tibetan Plateau has expanded northwards since 40 Ma (Rohrmann et al., 2012; C. Wang, Dai, et al., 2014) and may have intensified the Siberian High and dust transport (C. Zhu et al., 2019). However, it remains unclear whether this long-term process could have resulted in the abrupt shifts observed at 40 Ma in the Xining Basin.

Finally, we consider the sea incursions of the inland proto-Paratethys Sea (Figure 10). Recent studies constrained the extent and timing of these sea incursions and dated a major sea retreat to ~41–40 Ma (Kaya

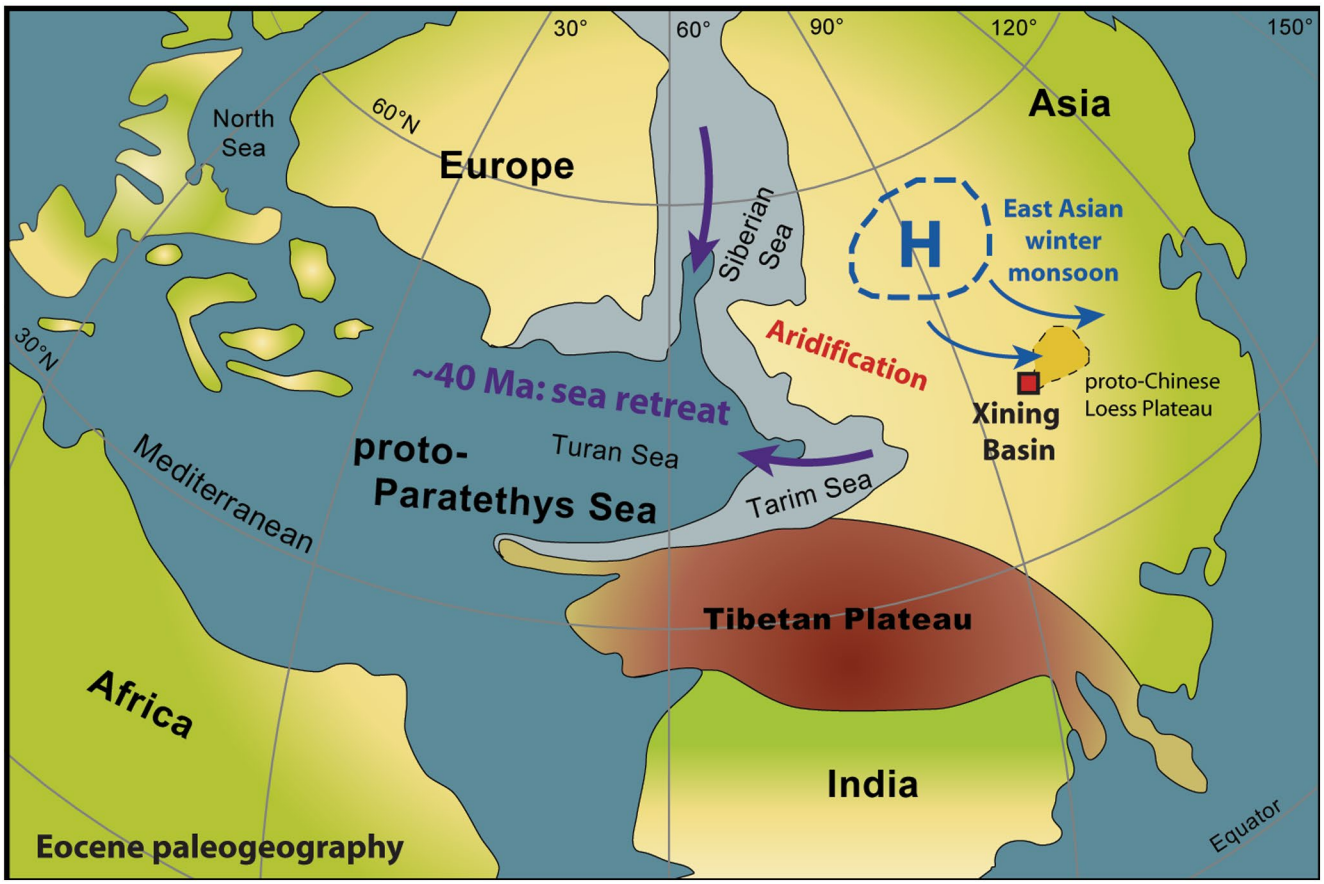

Figure 10. Eocene paleogeography of Eurasia (modified from Bosboom et al., 2011) showing the retreat of the proto-Paratethys Sea. This may have resulted in aridification and the onset of a high-pressure system over Siberia driving the East Asian winter monsoon and dust storms in the Xining Basin.

et al., 2019), coeval with the shifts in the Xining Basin. Sensitivity climate model simulations using various paleogeographies of the proto-Paratethys Sea show that the Asian climate is especially sensitive to this particular sea retreat from the Tarim and Siberian Sea (Z. Zhang et al., 2007). According to these simulations, this regression acts as a tipping point resulting in both the strengthening of a high-pressure system over Siberia due to increased continentality as well as the aridification of northwestern China by removing a major moisture source for this region (Figure 10). Although the aridification itself can explain the observed shifts in vegetation and the increase in dust at 40 Ma, it does not explain the onset of obliquity cycles and the northwesterly wind directions. Therefore, we propose that the sea retreat driving the appearance of the Siberian High is the most plausible mechanism to explain the shifts observed in the Xining Basin. However, it should be noted that other mechanisms such as atmospheric cooling and Tibetan Plateau uplift may have played a role as well and should be tested by future climate model simulations.

8.3. Regional Aridification and Dust Records

The onset of dust in the Xining Basin precedes the eolian deposits observed in most other regions of Central Asia, except for a poorly dated record at ~51 Ma in the Xorkol Basin (Li et al., 2018), which is located outside of the Loess Plateau region and likely driven by a different atmospheric configuration. Dust is observed to significantly increase in the grain-size record of the neighboring Lanzhou Basin at ~26 Ma (Y. Zhang et al., 2014). However, a recent reanalysis of this magnetostratigraphic record suggests a dust increase at ~40 Ma (Wang et al., 2016), coeval with that observed in the Xining Basin and therefore suggesting a regional signal. Sedimentary records from Tajikistan show eolian dunes and loess shortly after the third Paleogene regression of the proto-Paratethys Sea (Carrapa et al., 2015), dated at 36.7 Ma (Kaya et al., 2019). The onset

of loess in Mongolia as well as eolian dunes in the Tarim Basin are observed at 34 Ma and are linked to the final retreat of the proto-Paratethys Sea at the EOT (Blayney et al., 2019; J. Sun & Windley, 2015). These records suggest that the continued retreat of the proto-Paratethys Sea resulted in the desertification of western Central Asia. Subsequent aridification due to atmospheric cooling and uplift during the Miocene may have progressively enhanced dust accumulation on the Chinese Loess Plateau as observed by the onset of dust at 26–20 Ma in the western part (Garzione et al., 2005; Guo et al., 2002; Jiang & Ding, 2010; X. Qiang et al., 2011; W. T. Wang et al., 2011) and at 11-8 Ma in the eastern part (Ao et al., 2016; Sun et al., 1998; B. Wang, Zheng, et al., 2014). Alternatively, these basal ages may reflect a tectonic control on the accommodation and preservation of loess rather than an atmospheric shift (B. Wang et al., 2018).

A poorly dated record from the eastern Pacific Ocean reveals the appearance of a minor detrital dust component between 50 and 40 Ma, followed by a large increase of this component at 20 Ma (Ziegler et al., 2007). Provenance data show that the northern Pacific Ocean is dominated by Asian dust since 40 Ma (Pettke et al., 2002). Dust accumulation rates of this record are low during the Cenozoic followed by a doubling at 25 Ma and an even larger increase in accumulation rate at 3–4 Ma (Janecek & Rea, 1983). However, a recent study with improved age constraints suggests that the accumulation rates increased continuously since at least 25 Ma rather than stepwise (W. Zhang, Chen, et al., 2016). These records add to the notion for the onset of an initial dust component at 40 Ma followed by a progressive aridification of the Asian interior resulting in a large increase in dust accumulation during the late Oligocene to early Miocene.

9. Conclusions

We identified the appearance of a loess-like dust component in the terrestrial record of the Xining Basin at 40 Ma, coeval with the onset of obliquity cycles and a shift to dominance of steppe-desert vegetation previously identified by Bosboom et al. (2014). We propose that these shifts are linked to retreat of the proto-Paratethys Sea which, in addition to the long-term Tibetan Plateau uplift and global cooling, may have set up the Siberian High resulting in winter monsoonal circulation and associated dust storms. This obliquity-driven high-pressure system would have deflected westerly moisture and driven the cyclicity observed in the Xining Basin as well as regional aridification and corresponding biotic shifts. However, more Central Asian records are needed to confirm that the 40 Ma events are indeed a regional signal. Our study suggests that the Siberian High may have driven cold surges over eastern Asia since 40 Ma and should be taken into account when reconstructing temperatures in this region (Tang et al., 2015). Middle to late Eocene Asian dust may have played a critical role in the global cooling and set-up of the greenhouse to icehouse transition by scattering incoming radiation, promoting the formation of clouds and affecting the carbon cycle by fertilizing phytoplankton production in the Pacific Ocean (Jickells et al., 2005; Martin, 1990; Shaffer & Lambert, 2018). Especially because middle to late Eocene loessites have been identified in South and North America as well (Bellosi, 2010; M. Fan et al., 2020). The role of this Eocene dust as well as the mechanisms driving the Siberian High should be further explored and tested in future proxy records and climate modeling studies.

Data Availability Statement

Raw paleomagnetic data is available at earthref.org/MagIC/16967 and ChRM directions, grain-size, cyclostratigraphic (XRF and color) and palynological data are available at https://doi.pangaea.de/10.1594/PANGAEA.923996 as well as in the Supporting Information.

Acknowledgments
This work was funded by the ERC consolidator grant MAGIC 649081 to GDN. We thank Meimei Xiao, Aijun Sun, Zhipeng Wu, Shengcheng Liu and for their help in the field and logistical support. We also thank Stefan Liening and Caroline Zorn for their help in the SedLab. We are grateful to Hans van Hateren for providing his Matlab script to calculate the class-wise R^2 of the end-members. We thank Peter Selkin, Daniel E. Ibarra and five anonymous reviewers for their comments and feedback. Open Access funding enabled and organized by Projekt DEAL.

References

Abels, H. A., Aziz, H. A., Krijgsman, W., Smeets, S. J., & Hilgen, F. J. (2010). Long-period eccentricity control on sedimentary sequences in the continental Madrid Basin (middle Miocene, Spain). *Earth and Planetary Science Letters*, *289*(1–2), 220–231. https://doi.org/10.1016/j.epsl.2009.11.011

Abels, H. A., Dupont-Nivet, G., Xiao, G., Bosboom, R., & Krijgsman, W. (2011). Step-wise change of Asian interior climate preceding the Eocene–Oligocene Transition (EOT). *Palaeogeography, Palaeoclimatology, Palaeoecology*, *299*(3), 399–412. https://doi.org/10.1016/j.palaeo.2010.11.028

Alonso-Zarza, A. M., Zhao, Z., Song, C. H., Li, J. J., Zhang, J., Martín-Pérez, A., et al. (2009). Mudflat/distal fan and shallow lake sedimentation (upper Vallesian–Turolian) in the Tianshui Basin, Central China: Evidence against the late Miocene eolian loess. *Sedimentary Geology*, *222*(1–2), 42–51. https://doi.org/10.1016/j.sedgeo.2009.03.010

An, Z., Kutzbach, J. E., Prell, W. L., & Porter, S. C. (2001). Evolution of Asian monsoons and phased uplift of the Himalaya–Tibetan plateau since Late Miocene times. *Nature*, *411*(6833), 62. https://doi.org/10.1038/35075035

Ao, H., Roberts, A. P., Dekkers, M. J., Liu, X., Rohling, E. J., Shi, Z., et al. (2016). Late Miocene–Pliocene Asian monsoon intensification linked to Antarctic ice-sheet growth. *Earth and Planetary Science Letters*, *444*, 75–87. https://doi.org/10.1016/j.epsl.2016.03.028

Barbolini, N., Woutersen, A., Dupont-Nivet, G., Silvestro, D., Tardif, D., Meijer, N., et al. (2020). Cenozoic evolution of the steppe-desert biome in Central Asia. *Science Advances*, *6*(41), eabb8227. https://doi.org/10.1126/sciadv.abb8227

Bellosi, E. S. (2010). Physical stratigraphy of the Sarmiento Formation (middle Eocene–lower Miocene) at Gran Barranca, central Patagonia. R. H. Madden A. A. Carlini M. G. Vucetich & R. F. Kay (Eds.), In *The paleontology of Gran Barranca* (pp. 19–31). New York, NY: Cambridge University.

Blayney, T., Dupont-Nivet, G., Najman, Y., Proust, J. N., Meijer, N., Roperch, P., et al. (2019). Tectonic evolution of the Pamir recorded in the Western Tarim Basin (China): Sedimentologic and magnetostratigraphic analyses of the Aertashi section. *Tectonics*, *38*, 492–515. https://doi.org/10.1029/2018TC005146

Bosboom, R. E., Abels, H. A., Hoorn, C., van den Berg, B. C., Guo, Z., & Dupont-Nivet, G. (2014). Aridification in continental Asia after the Middle Eocene Climatic Optimum (MECO). *Earth and Planetary Science Letters*, *389*, 34–42. https://doi.org/10.1016/j.epsl.2013.12.014

Bosboom, R. E., Dupont-Nivet, G., Houben, A. J., Brinkhuis, H., Villa, G., Mandic, O., et al. (2011). Late Eocene sea retreat from the Tarim Basin (west China) and concomitant Asian paleoenvironmental change. *Palaeogeography, Palaeoclimatology, Palaeoecology*, *299*(3–4), 385–398. https://doi.org/10.1016/j.palaeo.2010.11.019

Bosmans, J. H. C., Erb, M. P., Dolan, A. M., Drijfhout, S. S., Tuenter, E., Hilgen, F. J., et al. (2018). Response of the Asian summer monsoons to idealized precession and obliquity forcing in a set of GCMs. *Quaternary Science Reviews*, *188*, 121–135. https://doi.org/10.1016/j.quascirev.2018.03.025

Bureau of Geological and Mineral Resources of Qinghai Province (BGMRQP). (1965). In *Regional geological survey reports of Ledu sheet (1:200000), Qinghai Province, P.R. China*, Beijing: Geological Publishing House.

Carrapa, B., DeCelles, P. G., Wang, X., Clementz, M. T., Mancin, N., Stoica, M., et al. (2015). Tectono-climatic implications of Eocene Paratethys regression in the Tajik basin of central Asia. *Earth and Planetary Science Letters*, *424*, 168–178. https://doi.org/10.1016/j.epsl.2015.05.034

Chang, C. P., Wang, Z., & Hendon, H. (2006). The Asian winter monsoon. Bin Wang (Ed.) In *The Asian monsoon* (pp. 89–127). Berlin, Heidelberg: Springer. https://doi.org/10.1007/3-540-37722-0_3

Cramwinckel, M. J., Huber, M., Kocken, I. J., Agnini, C., Bijl, P. K., Bohaty, S. M., et al. (2018). Synchronous tropical and polar temperature evolution in the Eocene. *Nature*, *559*(7714), 382. https://doi.org/10.1038/s41586-018-0272-2

Dai, S., Fang, X., Dupont-Nivet, G., Song, C., Gao, J., Krijgsman, W., et al. (2006). Magnetostratigraphy of Cenozoic sediments from the Xining Basin: Tectonic implications for the northeastern Tibetan Plateau. *Journal of Geophysical Research*, *111*(B11), 102. https://doi.org/10.1029/2005JB004187

Dietze, E., & Dietze, M. (2019). Grain-size distribution unmixing using the R package EMMAgeo. *E&G-Quaternary Science Journal*, *68*, 29–46. https://doi.org/10.5194/egqsj-68-29-2019

Dietze, E., Maussion, F., Ahlborn, M., Diekmann, B., Hartmann, K., Henkel, K., et al. (2014). Sediment transport processes across the Tibetan Plateau inferred from robust grain-size end members in lake sediments. *Climate of the Past*, *10*(1), 91–106. https://doi.org/10.5194/cp-10-91-2014

Ding, Z., Rutter, N. W., & Liu, T. (1997). The onset of extensive loess deposition around the G/M boundary in China and its palaeoclimatic implications. *Quaternary International*, *40*, 53–60. https://doi.org/10.1016/S1040-6182(96)00061-4

Ding, Z. L., Sun, J. M., Yang, S. L., & Liu, T. S. (1998). Preliminary magnetostratigraphy of a thick eolian red clay-loess sequence at Lingtai, the Chinese Loess Plateau. *Geophysical Research Letters*, *25*(8), 1225–1228. https://doi.org/10.1029/98GL00836

Ding, Z. L., Yang, S. L., Hou, S. S., Wang, X., Chen, Z., & Liu, T. S. (2001). Magnetostratigraphy and sedimentology of the Jingchuan red clay section and correlation of the Tertiary eolian red clay sediments of the Chinese Loess Plateau. *Journal of Geophysical Research*, *106*(B4), 6399–6407. https://doi.org/10.1029/2000JB900445

Dupont-Nivet, G., Dai, S., Fang, X., Krijgsman, W., Erens, V., Reitsma, M., & Langereis, C. (2008). Timing and distribution of tectonic rotations in the northeastern Tibetan Plateau. *Investigations into the Tectonics of the Tibetan Plateau*, *444*, 73–87.

Dupont-Nivet, G., Hoorn, C., & Konert, M. (2008). Tibetan uplift prior to the Eocene-Oligocene climate transition: Evidence from pollen analysis of the Xining Basin. *Geology*, *36*(12), 987–990. https://doi.org/10.1130/G25063A.1

Dupont-Nivet, G., Krijgsman, W., Langereis, C. G., Abels, H. A., Dai, S., & Fang, X. (2007). Tibetan plateau aridification linked to global cooling at the Eocene–Oligocene transition. *Nature*, *445*(7128), 635–638. https://doi.org/10.1038/nature05516

Fan, M., Feng, R., Geissman, J. W., & Poulsen, C. J. (2020). Late Paleogene emergence of a North American loess plateau. *Geology*, *48*(3), 273–277. https://doi.org/10.1130/G47102.1

Fang, X., Fang, Y., Zan, J., Zhang, W., Song, C., Appel, E., et al. (2019). Cenozoic magnetostratigraphy of the Xining Basin, NE Tibetan Plateau, and its constraints on paleontological, sedimentological and tectonomorphological evolution. *Earth-Science Reviews*, *190*, 460–485. https://doi.org/10.1016/j.earscirev.2019.01.021

Fan, L. G., Meng, Q. R., Wu, G. L., Wei, H. H., Du, Z. M., & Wang, E. (2019). Paleogene crustal extension in the eastern segment of the NE Tibetan plateau. *Earth and Planetary Science Letters*, *514*, 62–74. https://doi.org/10.1016/j.epsl.2019.02.036

Farnsworth, A., Lunt, D. J., Robinson, S. A., Valdes, P. J., Roberts, W. H., Clift, P. D., et al. (2019). Past East Asian monsoon evolution controlled by paleogeography, not CO2. *Science Advances*, *5*(10), eaax1697. https://doi.org/10.1126/sciadv.aax1697

Fisher, R. (1953). Dispersion on a sphere. *Proceedings of the Royal Society of London A: Mathematical, Physical and Engineering Sciences*, *217*(1130), 295–305. https://doi.org/10.1098/rspa.1953.0064

Garzione, C. N., Ikari, M. J., & Basu, A. R. (2005). Source of Oligocene to Pliocene sedimentary rocks in the Linxia basin in northeastern Tibet from Nd isotopes: Implications for tectonic forcing of climate. *GSA Bulletin*, *117*(9–10), 1156–1166. https://doi.org/10.1130/B25743.1

Goossens, D. (2008). Techniques to measure grain-size distributions of loamy sediments: a comparative study of ten instruments for wet analysis. *Sedimentology*, *55*(1), 65–96. https://doi.org/10.1111/j.1365-3091.2007.00893.x

Gradstein, F. M., Ogg, J. G., Schmitz, J. G., & Ogg, G. (Eds.), (2012). *The geologic time scale 2012*. Elsevier.

Guo, Z. T., Ruddiman, W. F., Hao, Q. Z., Wu, H. B., Qiao, Y. S., Zhu, R. X., et al. (2002). Onset of Asian desertification by 22 Myr ago inferred from loess deposits in China. *Nature*, *416*(6877), 159. https://doi.org/10.1038/416159a

Hammer, Ø., Harper, D. A., & Ryan, P. D. (2001). PAST: Paleontological statistics software package for education and data analysis. *Palaeontologia Electronica*, *4*(1), 9.

Hoorn, C., Straathof, J., Abels, H. A., Xu, Y., Utescher, T., & Dupont-Nivet, G. (2012). A late Eocene palynological record of climate change and Tibetan Plateau uplift (Xining Basin, China). *Palaeogeography, Palaeoclimatology, Palaeoecology*, *344*, 16–38. https://doi.org/10.1016/j.palaeo.2012.05.011

Horton, B. K., Dupont-Nivet, G., Zhou, J., Waanders, G. L., Butler, R. F., & Wang, J. (2004). Mesozoic-Cenozoic evolution of the Xining-Minhe and Dangchang basins, northeastern Tibetan Plateau: Magnetostratigraphic and biostratigraphic results. *Journal of Geophysical Research*, *109*(B4), 402. https://doi.org/10.1029/2003JB002913

Huang, C., & Hinnov, L. (2019). Astronomically forced climate evolution in a saline lake record of the middle Eocene to Oligocene, Jianghan Basin, China. *Earth and Planetary Science Letters*, *528*, 115846. https://doi.org/10.1016/j.epsl.2019.115846

Huber, M., & Goldner, A. (2012). Eocene monsoons. *Journal of Asian Earth Sciences*, *44*, 3–23. https://doi.org/10.1016/j.jseaes.2011.09.014

Janecek, T. R., & Rea, D. K. (1983). Eolian deposition in the northeast Pacific Ocean: Cenozoic history of atmospheric circulation. *The Geological Society of America Bulletin*, *94*(6), 730–738. https://doi.org/10.1130/0016-7606(1983)94<730:EDITNP>2.0.CO;2

Jansonius, J., & Hills, L. V. (1976). *Genera file of fossil spores and pollen special publication*. Calgary, Canada: Department of Geology, University of Calgary.

Jiang, H., & Ding, Z. (2010). Eolian grain-size signature of the Sikouzi lacustrine sediments (Chinese Loess Plateau): Implications for Neogene evolution of the East Asian winter monsoon. *Bulletin*, *122*(5–6), 843–854. https://doi.org/10.1130/B26583.1

Jickells, T. D., An, Z. S., Andersen, K. K., Baker, A. R., Bergametti, G., Brooks, N., et al. (2005). Global iron connections between desert dust, ocean biogeochemistry, and climate. *Science*, *308*(5718), 67–71.

Kaya, M. Y., Dupont-Nivet, G., Proust, J.-N., Roperch, P., Bougeois, L., Meijer, N., et al. (2019). Paleogene evolution and demise of the proto-Paratethys Sea in Central Asia (Tarim and Tajik basins): Role of intensified tectonic activity at ~41 Ma. *Basin Research*, *31*(3), 461–486. https://doi.org/10.1111/bre.12330

Kirschvink, J. L. (1980). The least-squares line and plane and the analysis of palaeomagnetic data. *Geophysical Journal International*, *62*(3), 699–718. https://doi.org/10.1111/j.1365-246X.1980.tb02601.x

Kocken, I. J., Cramwinckel, M. J., Zeebe, R., Middelburg, J. B. M., & Sluijs, A. (2019). The 405 kyr and 2.4 Myr eccentricity components in Cenozoic carbon isotope records. *Climate of the Past*, *15*(1), 91–104. https://doi.org/10.5194/cp-15-91-2019

Krinsley, D. H., & McCoy, F. W. (1977). Significance and origin of surface textures on broken sand grains in deep-sea sediments. *Sedimentology*, *24*(6), 857–862. https://doi.org/10.1111/j.1365-3091.1977.tb01920.x

Laskar, J., Fienga, A., Gastineau, M., & Manche, H. (2011). La2010: A new orbital solution for the long-term motion of the Earth. *Astronomy & Astrophysics*, *532*, A89. https://doi.org/10.1051/0004-6361/201116836

Licht, A., Dupont-Nivet, G., Meijer, N., Rugenstein, J. C., Schauer, A., Fiebig, J., et al. (2020). Decline of soil respiration in northeastern Tibet through the transition into the Oligocene icehouse. *Palaeogeography, Palaeoclimatology, Palaeoecology*, *560*, 110016. https://doi.org/10.1016/j.palaeo.2020.110016

Licht, A., Dupont-Nivet, G., Pullen, A., Kapp, P., Abels, H. A., Lai, Z., et al. (2016). Resilience of the Asian atmospheric circulation shown by Paleogene dust provenance. *Nature Communications*, *7*, 12390. https://doi.org/10.1038/ncomms12390

Licht, A., Van Cappelle, M., Abels, H. A., Ladant, J. B., Trabucho-Alexandre, J., France-Lanord, C., et al. (2014). Asian monsoons in a late Eocene greenhouse world. *Nature*, *513*(7519), 501–506. https://doi.org/10.1038/nature13704

Liu, S., Li, J., Stockli, D. F., Song, C., Guo, B., Stockli, L. D., et al. (2019). *Reappraisal of Miocene eolian deposition in Tianshui Basin, China, based on an investigation of stratigraphy and provenance*. Geological Society of America Bulletin. https://doi.org/10.1130/B32056.1

Liu, S., Zhang, G., Pan, F., Zhang, H., Wang, P., Wang, K., & Wang, Y. (2013). Timing of Xunhua and Guide basin development and growth of the northeastern Tibetan Plateau, China. *Basin Research*, *25*(1), 74–96. https://doi.org/10.1111/j.1365-2117.2012.00548.x

Li, J. X., Yue, L. P., Roberts, A. P., Hirt, A. M., Pan, F., Guo, L., et al. (2018). Global cooling and enhanced Eocene Asian mid-latitude interior aridity. *Nature Communications*, *9*(1), 3026. https://doi.org/10.1038/s41467-018-05415-x

Lu, H., Wang, X., & Li, L. (2010). Aeolian sediment evidence that global cooling has driven late Cenozoic stepwise aridification in central Asia. *Geological Society, London, Special Publications*, *342*(1), 29–44. https://doi.org/10.1144/SP342.4

Maher, B. A. (2016). Palaeoclimatic records of the loess/palaeosol sequences of the Chinese Loess Plateau. *Quaternary Science Reviews*, *154*, 23–84. https://doi.org/10.1016/j.quascirev.2016.08.004

Martin, J. H. (1990). Glacial-interglacial CO2 change: The iron hypothesis. *Paleoceanography*, *5*(1), 1–13. https://doi.org/10.1029/PA005i001p00001

McFadden, P. L., & McElhinny, M. W. (1990). Classification of the reversal test in palaeomagnetism. *Geophysical Journal International*, *103*(3), 725–729. https://doi.org/10.1111/j.1365-246X.1990.tb05683.x

McKee, E. D. (1966). Structures of dunes at White Sands National Monument, New Mexico (and a comparison with structures of dunes from other selected areas) 1. *Sedimentology*, *7*(1), 3–69. https://doi.org/10.1111/j.1365-3091.1966.tb01579.x

Meijer, N., Dupont-Nivet, G., Abels, H. A., Kaya, M. Y., Licht, A., Xiao, M., et al. (2019). Central Asian moisture modulated by proto-Paratethys Sea incursions since the early Eocene. *Earth and Planetary Science Letters*, *510*, 73–84. https://doi.org/10.1016/j.epsl.2018.12.031

Meijer, N., Dupont-Nivet, G., Licht, A., Trabucho-Alexandre, J., Bourquin, S., & Abels, H. A. (2020). Identifying eolian dust in the geological record. *Earth-Science Reviews*, *211*, 103410. https://doi.org/10.1016/j.earscirev.2020.103410

Nie, J., King, J. W., & Fang, X. (2008). Tibetan uplift intensified the 400 ky signal in paleoclimate records at 4 Ma. *The Geological Society of America Bulletin*, *120*(9–10), 1338–1344. https://doi.org/10.1130/B26349.1

Nie, J., Peng, W., Möller, A., Song, Y., Stockli, D. F., Stevens, T., et al. (2014). Provenance of the upper Miocene–Pliocene Red Clay deposits of the Chinese loess plateau. *Earth and Planetary Science Letters*, *407*, 35–47. https://doi.org/10.1016/j.epsl.2014.09.026

North, C. P., & Davidson, S. K. (2012). Unconfined alluvial flow processes: recognition and interpretation of their deposits, and the significance for palaeogeographic reconstruction. *Earth-Science Reviews*, *111*(1), 199–223. https://doi.org/10.1016/j.earscirev.2011.11.008

Ogg, J. G., Ogg, G., & Gradstein, F. M. (2016). *A concise geologic time scale: 2016*. Elsevier.

Page, M., Licht, A., Dupont-Nivet, G., Meijer, N., Barbolini, N., Hoorn, C., et al. (2019). Synchronous cooling and decline in monsoonal rainfall in northeastern Tibet during the fall into the Oligocene icehouse. *Geology*, *47*(3), 203–206. https://doi.org/10.1130/G45480.1

Paillard, D., Labeyrie, L. D., & Yiou, P. (1996). AnalySeries 1.0: A Macintosh software for the analysis of geophysical time-series. *EOS*, *77*, 379.

Paterson, G. A., & Heslop, D. (2015). New methods for unmixing sediment grain size data. *Geochemistry, Geophysics, Geosystems*, *16*(12), 4494–4506. https://doi.org/10.1002/2015GC006070

Pettke, T., Halliday, A. N., & Rea, D. K. (2002). Cenozoic evolution of Asian climate and sources of Pacific seawater Pb and Nd derived from eolian dust of sediment core LL44-GPC3. *Paleoceanography*, *17*(3), 1–13. https://doi.org/10.1029/2001PA000673

Pye, K. (1995). The nature, origin and accumulation of loess. *Quaternary Science Reviews*, *14*(7–8), 653–667. https://doi.org/10.1016/0277-3791(95)00047-X

Qiang, X. K., Li, Z. X., Powell, C. M., & Zheng, H. B. (2001). Magnetostratigraphic record of the Late Miocene onset of the East Asian monsoon, and Pliocene uplift of northern Tibet. *Earth and Planetary Science Letters*, *187*(1-2), 83–93. https://doi.org/10.1016/S0012-821X(01)00281-3

Qiang, X., An, Z., Song, Y., Chang, H., Sun, Y., Liu, W., et al. (2011). New eolian red clay sequence on the western Chinese Loess Plateau linked to onset of Asian desertification about 25 Ma ago. *Science China Earth Sciences*, *54*(1), 136–144. https://doi.org/10.1007/s11430-010-4126-5

Qiang, M., Lang, L., & Wang, Z. (2010). Do fine-grained components of loess indicate westerlies: Insights from observations of dust storm deposits at Lenghu (Qaidam Basin, China). *Journal of Arid Environments*, *74*(10), 1232–1239. https://doi.org/10.1016/j.jaridenv.2010.06.002

Qinghai Bureau of Geology and Mineral Resources (QBGMR). (1985). *Geologic maps of the Duoba, Gaodian, Tianjiazai, and Xining regions (4 sheets), with regional geologic report (1:50,000 scale)* (p. 199). Beijing, China: Geological Publishing House.

Roe, G. (2009). On the interpretation of Chinese loess as a paleoclimate indicator. *Quaternary Research*, *71*(2), 150–161. https://doi.org/10.1016/j.yqres.2008.09.004

Rohrmann, A., Kapp, P., Carrapa, B., Reiners, P. W., Guynn, J., Ding, L., & Heizler, M. (2012). Thermochronologic evidence for plateau formation in central Tibet by 45 Ma. *Geology*, *40*(2), 187–190. https://doi.org/10.1130/G32530.1

Schulz, M., & Mudelsee, M. (2002). REDFIT: Estimating red-noise spectra directly from unevenly spaced paleoclimatic time series. *Computers & Geosciences*, *28*(3), 421–426. https://doi.org/10.1016/S0098-3004(01)00044-9

Shaffer, G., & Lambert, F. (2018). In and out of glacial extremes by way of dust— climate feedbacks. *Proceedings of the National Academy of Sciences*, *115*(9), 2026–2031. https://doi.org/10.1073/pnas.1708174115

Shang, Y., Beets, C. J., Tang, H., Prins, M. A., Lahaye, Y., van Elsas, R., et al. (2016). Variations in the provenance of the late Neogene Red Clay deposits in northern China. *Earth and Planetary Science Letters*, *439*, 88–100. https://doi.org/10.1016/j.epsl.2016.01.031

Sha, Y., Shi, Z., Liu, X., & An, Z. (2015). Distinct impacts of the Mongolian and Tibetan Plateaus on the evolution of the East Asian monsoon. *Journal of Geophysical Research: Atmospheres*, *120*(10), 4764–4782. https://doi.org/10.1002/2014JD022880

Shi, Z. G., Liu, X. D., Sun, Y. B., An, Z. S., Liu, Z., & Kutzbach, J. (2011). Distinct responses of East Asian summer and winter monsoons to astronomical forcing. *Climate of the Past*, *7*(4), 1363–1370. https://doi.org/10.5194/cp-7-1363-2011

Smoot, J. P., & Lowenstein, T. K. (1991). Depositional environments of non-marine evaporites. *Developments in Sedimentology*, *50*, 189–347. https://doi.org/10.1016/S0070-4571(08)70261-9

Song, Y., Fang, X., Masayuki, T., Naoto, I., Li, J., & An, Z. (2001). Magnetostratigraphy of Late Tertiary sediments from the Chinese Loess Plateau and its paleoclimatic significance. *Chinese Science Bulletin*, *46*(1), 16–21. https://doi.org/10.1007/BF03187230

Song, Z. C., Zheng, Y., Li, M., Zhang, Y., Wang, W., Wang, D., et al. (1999). Fossil spores and pollen of China Vol 1. In The late Cretaceous and Tertiary spores and pollen (Vol. 17, pp. 910). Beijing: Science Press.

Sperazza, M., Moore, J. N., & Hendrix, M. S. (2004). High-resolution particle size analysis of naturally occurring very fine-grained sediment through laser diffractometry. *Journal of Sedimentary Research*, *74*(5), 736–743. https://doi.org/10.1306/031104740736

Sun, J. (2002). Provenance of loess material and formation of loess deposits on the Chinese Loess Plateau. *Earth and Planetary Science Letters*, *203*(3–4), 845–859. https://doi.org/10.1016/S0012-821X(02)00921-4

Sun, D., An, Z., Shaw, J., Bloemendal, J., & Sun, Y. (1998). Magnetostratigraphy and palaeoclimatic significance of Late Tertiary aeolian sequences in the Chinese Loess Plateau. *Geophysical Journal International*, *134*(1), 207–212. https://doi.org/10.1046/j.1365-246x.1998.00553.x

Sun, D., Liu, D., Chen, M., An, Z., & John, S. (1997). Magnetostratigraphy and palaeoclimate of red clay sequences from Chinese Loess Plateau. *Science in China - Series D: Earth Sciences*, *40*(4), 337–343. https://doi.org/10.1007/BF02877564

Sun, D., Shaw, J., An, Z., Cheng, M., & Yue, L. (1998). Magnetostratigraphy and paleoclimatic interpretation of a continuous 7.2 Ma Late Cenozoic eolian sediments from the Chinese Loess Plateau. *Geophysical Research Letters*, *25*(1), 85–88. https://doi.org/10.1029/97GL03353

Sun, J., & Windley, B. F. (2015). Onset of aridification by 34 Ma across the Eocene-Oligocene transition in Central Asia. *Geology*, *43*(11), 1015–1018. https://doi.org/10.1130/G37165.1

Talbot, M. R., Holm, K., & Williams, M. A. J. (1994). Sedimentation in low-gradient desert margin systems: A comparison of the Late Triassic of northwest Somerset (England) and the late Quaternary of east-central Australia. *Geological Society of America Special Papers*, *289*, 97–117.

Tang, H., Eronen, J. T., Kaakinen, A., Utescher, T., Ahrens, B., & Fortelius, M. (2015). Strong winter monsoon wind causes surface cooling over India and China in the Late Miocene. *Climate of the Past Discussions*, *11*(1), 63–93. https://doi.org/10.5194/cpd-11-63-2015

Tardif, D., Fluteau, F., Donnadieu, Y., Le Hir, G., Ladant, J. B., Sepulchre, P., et al. (2020). The origin of Asian monsoons: A modelling perspective. *Climate of the Past*, *16*(3), 847–865. https://doi.org/10.5194/cp-16-847-2020

Tripati, A., & Darby, D. (2018). Evidence for ephemeral middle Eocene to early Oligocene Greenland glacial ice and pan-Arctic sea ice. *Nature Communications*, *9*(1), 1038. https://doi.org/10.1038/s41467-018-03180-5

Újvári, G., Kok, J. F., Varga, G., & Kovács, J. (2016). The physics of wind-blown loess: Implications for grain size proxy interpretations in Quaternary paleoclimate studies. *Earth-Science Reviews*, *154*, 247–278. https://doi.org/10.1016/j.earscirev.2016.01.006

van Hateren, J. A., Prins, M. A., & van Balen, R. T. (2018). On the genetically meaningful decomposition of grain-size distributions: A comparison of different end-member modelling algorithms. *Sedimentary Geology*, *375*, 49–71. https://doi.org/10.1016/j.sedgeo.2017.12.003

van Toorenenburg, K. A., Donselaar, M. E., & Weltje, G. J. (2018). The life cycle of crevasse splays as a key mechanism in the aggradation of alluvial ridges and river avulsion. *Earth Surface Processes and Landforms*, *43*(11), 2409–2420. https://doi.org/10.1002/esp.4404

Vandenberghe, J. (2013). Grain size of fine-grained windblown sediment: A powerful proxy for process identification. *Earth-Science Reviews*, *121*, 18–30. https://doi.org/10.1016/j.earscirev.2013.03.001

Varga, G., Gresina, F., Újvári, G., Kovács, J., & Szalai, Z. (2019). On the reliability and comparability of laser diffraction grain size measurements of paleosols in loess records. *Sedimentary Geology*, *389*, 42–53. https://doi.org/10.1016/j.sedgeo.2019.05.011

Varga, G., Újvári, G., & Kovács, J. (2019). Interpretation of sedimentary (sub) populations extracted from grain size distributions of Central European loess-paleosol series. *Quaternary International*, *502*, 60–70. https://doi.org/10.1016/j.quaint.2017.09.021

Vassallo, R., Jolivet, M., Ritz, J. F., Braucher, R., Larroque, C. H., Sue, C., et al. (2007). Uplift age and rates of the Gurvan Bogd system (Gobi-Altay) by apatite fission track analysis. *Earth and Planetary Science Letters*, *259*(3–4), 333–346. https://doi.org/10.1016/j.epsl.2007.04.047

Ventra, D., Abels, H. A., Hilgen, F. J., & de Boer, P. L. (2018). Orbital-climate control of mass-flow sedimentation in a Miocene alluvial-fan succession (Teruel Basin, Spain). *Geological Society, London, Special Publications*, *440*(1), 129–157. https://doi.org/10.1144/SP440.14

Wang, C., Dai, J., Zhao, X., Li, Y., Graham, S. A., He, D., et al. (2014). Outward-growth of the Tibetan Plateau during the Cenozoic: A review. *Tectonophysics*, *621*, 1–43. https://doi.org/10.1016/j.tecto.2014.01.036

Wang, Z., Huang, C., Licht, A., Zhang, R., & Kemp, D. B. (2019). Middle to late Miocene eccentricity forcing on lake expansion in NE Tibet. *Geophysical Research Letters*, *46*, 6926–6935. https://doi.org/10.1029/2019GL082283

Wang, B., Kaakinen, A., & Clift, P. D. (2018). Tectonic controls of the onset of aeolian deposits in Chinese Loess Plateau—A preliminary hypothesis. *International Geology Review*, *60*(8), 945–955. https://doi.org/10.1080/00206814.2017.1362362

Wang, W. T., Zhang, P. Z., Kirby, E., Wang, L. H., Zhang, G. L., Zheng, D. W., & Chai, C. Z. (2011). A revised chronology for Tertiary sedimentation in the Sikouzi basin: Implications for the tectonic evolution of the northeastern corner of the Tibetan Plateau. *Tectonophysics*, *505*(1–4), 100–114. https://doi.org/10.1016/j.tecto.2011.04.006

Wang, W., Zhang, P., Liu, C., Zheng, D., Yu, J., Zheng, W., et al. (2016). Pulsed growth of the West Qinling at ~30 Ma in northeastern Tibet: Evidence from Lanzhou Basin magnetostratigraphy and provenance. *Journal of Geophysical Research: Solid Earth*, *121*(11), 7754–7774. https://doi.org/10.1002/2016JB013279

Wang, B., Zheng, H., He, Z., Wang, P., Kaakinen, A., & Zhou, X. (2014). Middle Miocene eolian sediments on the southern Chinese Loess Plateau dated by magnetostratigraphy. *Palaeogeography, Palaeoclimatology, Palaeoecology*, *411*, 257–266. https://doi.org/10.1016/j.palaeo.2014.07.007

Weltje, G. J., Bloemsma, M. R., Tjallingii, R., Heslop, D., Röhl, U., & Croudace, I. W. (2015). Prediction of geochemical composition from XRF core scanner data: a new multivariate approach including automatic selection of calibration samples and quantification of uncertainties. I. W. Croudace & R. G. Rothwell (Eds.) In *Micro-XRF studies of sediment cores* (pp. 507–534). Dordrecht: Springer. https://doi.org/10.1007/978-94-017-9849-5_21

Weltje, G. J., & Prins, M. A. (2003). Muddled or mixed? Inferring palaeoclimate from size distributions of deep-sea clastics. *Sedimentary Geology*, *162*(1–2), 39–62. https://doi.org/10.1016/S0037-0738(03)00235-5

Weltje, G. J., & Tjallingii, R. (2008). Calibration of XRF core scanners for quantitative geochemical logging of sediment cores: Theory and application. *Earth and Planetary Science Letters*, *274*(3–4), 423–438. https://doi.org/10.1016/j.epsl.2008.07.054

Westerhold, T., Röhl, U., Frederichs, T., Agnini, C., Raffi, I., Zachos, J. C., & Wilkens, R. H. (2017). Astronomical calibration of the Ypresian timescale: implications for seafloor spreading rates and the chaotic behavior of the solar system? *Climate of the Past*, *13*(9), 1129. https://doi.org/10.5194/cp-13-1129-2017

Westerhold, T., Röhl, U., Frederichs, T., Bohaty, S. M., & Zachos, J. C. (2015). Astronomical calibration of the geological timescale: Closing the middle Eocene gap. *Climate of the Past*, *11*(9), 1181–1195. https://doi.org/10.5194/cp-11-1181-2015

Wright, V. P., & Marriott, S. B. (2007). The dangers of taking mud for granted: lessons from Lower Old Red Sandstone dryland river systems of South Wales. *Sedimentary Geology*, *195*(1–2), 91–100. https://doi.org/10.1016/j.sedgeo.2006.03.028

Xiao, G. Q., Abels, H. A., Yao, Z. Q., Dupont-Nivet, G., & Hilgen, F. J. (2010). Asian aridification linked to the first step of the Eocene-Oligocene climate Transition (EOT) in obliquity-dominated terrestrial records (Xining Basin, China). *Climate of the Past*, *6*(4), 501–513. https://doi.org/10.5194/cp-6-501-2010

Xiao, G., Guo, Z., Dupont-Nivet, G., Lu, H., Wu, N., Ge, J., et al. (2012). Evidence for northeastern Tibetan Plateau uplift between 25 and 20Ma in the sedimentary archive of the Xining Basin, Northwestern China. *Earth and Planetary Science Letters*, *317*, 185–195. https://doi.org/10.1016/j.epsl.2011.11.008

Xu, Y., Yue, L., Li, J., Sun, L., Sun, B., Zhang, J., et al. (2009). An 11-Ma-old red clay sequence on the Eastern Chinese Loess Plateau. *Palaeogeography, Palaeoclimatology, Palaeoecology*, *284*(3–4), 383–391. https://doi.org/10.1016/j.palaeo.2009.10.023

Yang, R., Fang, X., Meng, Q., Zan, J., Zhang, W., Deng, T., et al. (2017). Paleomagnetic constraints on the middle Miocene-early Pliocene stratigraphy in the Xining Basin, NE Tibetan Plateau, and the geologic implications. *Geochemistry, Geophysics, Geosystems*, *18*(11), 3741–3757. https://doi.org/10.1002/2017GC006945

Yang, F., Guo, Z., Zhang, C., Abu Sadat Md, S., He, Z., & Deng, C. (2019). High-resolution Eocene magnetostratigraphy of the Xijigou section: Implications for the infilling process of Xining Basin, northeastern Tibetan Plateau. *Journal of Geophysical Research: Solid Earth*, *124*(8), 7588–7603. https://doi.org/10.1029/2019JB017624

Yu, E., Zhang, R., Jiang, D., Ramstein, G., Zhang, Z., & Sun, J. (2018). High-resolution simulation of Asian monsoon response to regional uplift of the Tibetan Plateau with regional climate model nested with global climate model. *Global and Planetary Change*, *169*, 34–47. https://doi.org/10.1016/j.gloplacha.2018.07.002

Zhang, W., Chen, J., Ji, J., & Li, G. (2016). Evolving flux of Asian dust in the North Pacific Ocean since the late Oligocene. *Aeolian Research*, *23*, 11–20. https://doi.org/10.1016/j.aeolia.2016.09.004

Zhang, X., Jin, L., Huang, W., & Chen, F. (2016). Forcing mechanisms of orbital-scale changes in winter rainfall over northwestern China during the Holocene. *The Holocene*, *26*(4), 549–555. https://doi.org/10.1177/0959683615612569

Zhang, H., Lu, H., Stevens, T., Feng, H., Fu, Y., Geng, J., & Wang, H. (2018). Expansion of Dust Provenance and Aridification of Asia Since∼ 7.2 Ma Revealed by Detrital Zircon U-Pb Dating. *Geophysical Research Letters*, *45*(24), 13–437. https://doi.org/10.1029/2018GL079888

Zhang, Y., Sun, D., Li, Z., Wang, F., Wang, X., Li, B., et al. (2014). Cenozoic record of aeolian sediment accumulation and aridification from Lanzhou, China, driven by Tibetan Plateau uplift and global climate. *Global and Planetary Change*, *120*, 1–15. https://doi.org/10.1016/j.gloplacha.2014.05.009

Zhang, Z., Wang, H., Guo, Z., & Jiang, D. (2007). What triggers the transition of palaeoenvironmental patterns in China, the Tibetan Plateau uplift or the Paratethys Sea retreat? *Palaeogeography, Palaeoclimatology, Palaeoecology*, *245*(3–4), 317–331. https://doi.org/10.1016/j.palaeo.2006.08.003

Zhang, J., Wang, Y., Zhang, B., & Zhang, Y. (2016). Tectonics of the Xining Basin in NW China and its implications for the evolution of the NE Qinghai-Tibetan Plateau. *Basin Research*, *28*(2), 159–182. https://doi.org/10.1111/bre.12104

Zhang, W., Zhang, T., Song, C., Appel, E., Miao, Z., Fang, Y., et al. (2017). Termination of fluvial-alluvial sedimentation in the Xining Basin, NE Tibetan Plateau, and its subsequent geomorphic evolution. *Geomorphology*, *297*, 86–99. https://doi.org/10.1016/j.geomorph.2017.09.008

Zheng, H., An, Z., & Shaw, J. (1992). New contributions to Chinese Plio-pleistocene magnetostratigraphy. *Physics of the Earth and Planetary Interiors*, *70*(3–4), 146–153. https://doi.org/10.1016/0031-9201(92)90177-W

Zhu, C., Meng, J., Hu, Y., Wang, C., & Zhang, J. (2019). East-central Asian climate evolved with the northward migration of the high proto-Tibetan Plateau. *Geophysical Research Letters*, *46*(14), 8397–8406. https://doi.org/10.1029/2019GL082703

Zhu, Y., Zhou, L., Mo, D., Kaakinen, A., Zhang, Z., & Fortelius, M. (2008). A new magnetostratigraphic framework for late Neogene Hipparion Red Clay in the eastern Loess Plateau of China. *Palaeogeography, Palaeoclimatology, Palaeoecology*, *268*(1–2), 47–57. https://doi.org/10.1016/j.palaeo.2008.08.001

Ziegler, C. L., Murray, R. W., Hovan, S. A., & Rea, D. K. (2007). Resolving eolian, volcanogenic, and authigenic components in pelagic sediment from the Pacific Ocean. *Earth and Planetary Science Letters*, *254*(3–4), 416–432. https://doi.org/10.1016/j.epsl.2006.11.049